NASA TECHNICAL MEMORANDUM

A STUDY OF INTERNAL DRAG OF SMALL-SCALE DUCTS AT

MACH NUMBER 4

Lawrence A. Graham and Lynn W. Hunton

Ames Research Center
Moffett Field, Calif. 94035

March 1972

A STUDY OF INTERNAL DRAG OF SMALL-SCALE
DUCTS AT MACH NUMBER 4

By Lawrence A. Graham and Lynn W. Hunton
Ames Research Center

ABSTRACT

An experimental investigation has been made to examine the applicability of methods used to determine internal drag of small ducts and to study some of the problems encountered in assessing momentum losses in such ducts. Test Mach-number ranged from 3.7 to 4.4 at angles of attack of 0 and 5 degrees and at a constant Reynolds number of 4.3 million per foot. The configurations represented small ducts used to simulate external aerodynamics of airbreathing propulsion systems and consisted of wing-nacelle models of ducts with circular, square, and rectangular inlets and with a two-dimensional inlet.

A	area
A_c	inlet capture area
a^*	critical speed of sound
b	wing span
C_D	internal-drag coefficient, $\dfrac{\text{internal drag}}{q_\infty S}$
D_{bal}	total drag indicated by a balance
D	internal drag
l	length
M	duct exit Mach number
M_∞	free-stream Mach number
m	duct exit mass flow
m_i	duct inlet mass flow
m_∞	free-stream mass flow $= \rho_\infty V_\infty A_\infty$
N	total number of annuli being considered
n	annulus identification (where n=0 indicates duct longitudinal center line)
P_B	base pressure
P_{CH}	flexure chamber pressure
p	duct exit static pressure
p_∞	free-stream static pressure
P_l	duct exit static pressure at the median radius of annulus n
P_{t_∞}	free-stream total pressure
P_{t_1}	duct exit total pressure upstream of probe bow-shockwave
p'	duct exit total pressure downstream of probe bow-shockwave

p'_n	duct exit total pressure downstream of probe bow-shockwave measured at the median radius of annulus n
p'_w	duct exit total pressure downstream of the probe bow-shockwave measured at the duct wall
q_∞	free-stream dynamic pressure
R	Reynolds number per foot
r_{c_n}	median radius of annulus n
r_{max}	maximum duct radius
S	reference area, 0.785 in.^{2}
S_{seal}	seal area, 0.247 in.^{2}
S_{sleeve}	base area of inner sleeve, 0.131 in^2
V	duct exit velocity
V_∞	free-stream velocity
x	distance measured parallel to the duct exit longitudinal center line
α	angle of attack, referenced to duct exit longitudinal center line
γ	gas constant
δ	boundary layer thickness
ρ	mass density at the duct exit
Δr	radial increment

Subscripts:

F	force
o	at duct longitudinal center line
P	pressure

Superscripts:

$-$ (bar) average value

A STUDY OF INTERNAL DRAG OF SMALL-SCALE

DUCTS AT MACH NUMBER 4

By Lawrence A. Graham and Lynn W. Hunton
Ames Research Center

SUMMARY

Flow characteristics near the exit of the ducts of several small-scale wing-nacelle combinations have been experimentally investigated in the Mach number range between 3.7 and 4.4 at angles of attack of 0 and 5 degrees and a constant Reynolds number of 4.3×10^6 per foot. The purposes of the investigation were: 1) to examine the applicability in the supersonic speed range of methods that have heretofore been used to assess internal drag of small ducts used to simulate external aero-dynamics of airbreathing propulsion systems; 2) to determine the major problems encountered in assessing momentum losses in small ducts; and 3) to develop methods which may be used to precisely identify flow characteristics in small ducts at speeds extending into the hypersonic speed range.

The results showed that detailed pressure surveys are required to accurately define the flow characteristics near the exit of most of the configurations studied for the conditions of this investigation. A circular duct at $\alpha = 0$ was the one exception.

The results also showed that the internal drag of a duct with a circular inlet and exit could be successfully obtained from direct force measurements on an internal sleeve in the model. Internal-drag coefficient determined from detailed pressure surveys and momentum relationships near the exit of the model is in good agreement with force results. Internal-drag coefficient determined from skin-friction calculations on the internal surface of this duct and a duct with a square inlet and exit agreed reasonably well with force results. It was found that internal-drag results determined from momentum relationships are very sensitive to errors in total-pressure measurements.

INTRODUCTION

A continuing need exists for aerodynamic research at supersonic and hypersonic speeds to provide data for airbreathing aircraft configurations for realistic appraisal of the future potential of such vehicles. At these speeds it is essential that wind tunnel models represent flight vehicles in all their principle details for proper assessment of the external aerodynamics. However, not only must external flow fields of flight vehicles be duplicated as nearly as possible but the internal flow

in wind tunnel models must be accurately accounted for to properly assess external aerodynamics. The internal drag of small ducts used to simulate external aerodynamics of airbreathing propulsion systems on airplane configurations may be large in comparison to the total external drag. For such cases internal drag cannot be neglected as it has been sometimes where the internal drag is relatively small at lower speeds but must be accurately determined if external aerodynamic parameters are to be properly assessed.

The problem of simulating external aerodynamics of full-scale configurations with small-scale wind tunnel models has long since been recognized, particularly when engine ducting is accommodated. The problem is further complicated when the ducts are small since precise determination of flow characteristics in ducting becomes increasingly difficult as size of ducting becomes smaller. The purposes of this investigation are: (1) to examine the applicability in the supersonic speed range of methods that have heretofore been used to determine internal drag of small ducts used to simulate external aerodynamics of airbreathing propulsion systems; (2) to determine the problems encountered in calculating momentum losses in small ducts and; (3) to develop methods, either experimental and/or analytical, which may be used to precisely identify flow characteristics in small ducts at speeds extending into the hypersonic speed range. Data are presented for several wing-nacelle combinations with different geometry. Tests were conducted at Mach numbers ranging from 3.7 to 4.4 with a Reynolds number of 4.3×10^6 per foot and angles of attack of 0 and 5 degrees.

APPARATUS AND TESTS

Wind Tunnel

Tests were conducted in the Ames 1- by 3-Foot Supersonic Wind Tunnel which is a continuous flow facility with a Mach number range from about 1.5 to 6.0. Free-stream Reynolds number may be varied between about 3×10^5 and 9×10^6 per foot.

Models and Equipment

Models which were used in this investigation are illustrated in figures 1 and 2. The configurations included two circular ducts, a square duct, a rectangular inlet duct, and a 2-dimensional inlet duct with ramps. The latter two ducts had simulated wing planes extending ahead of the inlets. This provided simulation of the flow field and boundary layer ingestion from a wing. A simulated wing plane was used with all models so the geometry at the exit of all the ducts (model base) would be the same except for the square duct. With this one exception, all models had circular exits 1 inch in diameter, but all exit areas were equal.

The two circular inlet duct models were essentially identical in internal and external geometries. One was a constant diameter cylindrical duct with a sharp leading edge with an exterior wedge angle of 10 degrees (see figures 2(a) and (b)). The second model, hereafter referred to as the force model, is shown in an isometric sectional view and a photograph in figures 3(a) and (b), respectively. This force model had a constant diameter internal sleeve, beginning 1/2 inch downstream of the inlet lip. This sleeve was supported separately from the outer wall of the model on flexures which were instrumented with electrical strain gages. A thin flexible diaphragm at the base of the model prevented flow between the inner sleeve and the outer wall of the model. The models were sting supported from the base as shown in figure 3(a). Pertinent dimensions are shown in figure 3(c). Pressure probes were also supported near the base of the model as shown in figure 3(a). A mechanism provided movement of the probes from wall-to-wall of the duct exits along any axis normal to the duct longitudinal center line and +180 degrees roll about the longitudinal axis of the probe support. The square duct model had a constant area from inlet to exit which was equal to the circular exit areas of the other ducts. Photographs and pertinent dimensions of this model are presented in figures 4(a), (b) and (c).

A photograph of the rectangular inlet duct model is shown in figure 5(a) and pertinent dimensions are given in figure 5(b). The inlet cross section was constant from the lip to a point approximately 1.4 inches downstream after which the transition from a rectangular to a circular section was made in 4.6 inches.

The two-dimensional inlet duct with ramps is shown photographically in figure 6(a) and schematically with pertinent dimensions in figure 6(b). Three configurations of this type were investigated (only one shown). Transition section length 1 between the inlet and circular section of the duct was different for each model as shown on figure 6(b). Except for the transition lengths, the three models were identical.

Tests

Detailed static- and total-pressure surveys were made across each duct in a plane one-half inch upstream of the duct exit instead of the exit plane in an effort to avoid possible base interference effects. Surveys extended from wall-to-wall along the vertical, 45°, and horizontal axes in a plane normal to the duct longitudinal axis. Static pressures were also recorded from orifices spaced at 90° increments around the wall of the duct (vertical and horizontal axes) for all except the force model. Base pressure for all models and flexure-chamber pressure for the force model were measured for all runs.

Axial forces on the internal sleeve of the force model were obtained from electrical strain gages mounted on supporting flexures. Tests

were conducted at angles of attack of 0 and 5 degrees primarily at a
Mach number of 4.06 and a Reynolds number of 4.3 million per foot.
A limited number of tests were made over a Mach number range from about
3.7 to 4.4. Tunnel total pressure was held constant for all runs at
49.1 psia.

Corrections

Axial forces on the internal sleeve of the force model, flexure-
chamber pressure, and base pressure were all measured simultaneously. The
force on the balance D_{bal} was then corrected for the differential pres-
sure across the sleeve seal at the model base and for the sleeve base
pressure to obtain the internal drag.

$$D = D_{bal} - (p_{CH}-p_B)S_{seal} + (p_B-p_\infty)S_{sleeve} \tag{1}$$

Base pressures determined at seven locations as shown in figure 7 are
essentially constant. Therefore, all base pressure corrections are based
upon only the two pressures measured on the vertical centerline axis.

Results

Results from experimental pressure measurements for the various
models are presented in figures 8 through 15. Static- and total-pressure
distributions (p and p') are shown in figures 8 through 11 for $M_\infty = 4.06$,
$\alpha = 0$. Distributions of exit Mach number M determined from measured
pressures are also shown for these models for $M_\infty = 4.06$, $\alpha = 0$ in figures
8,9 and 11. Static- and total-pressure distributions for $M_\infty = 4.06$.
$\alpha = 0$ and $5°$ are shown in figure 10.

Experimental results over a Mach number range from about 3.7 to
4.4 are presented for the circular models in figures 12 through 14.
Results obtained from the force model over this Mach number range at
$\alpha = 0$ and $5°$ are presented in figure 12. Skin friction drag calculated
for the internal surface of the circular duct is also shown in this
figure. In figures 13 and 14, distributions of measured static- and total-
pressures (p and p' respectively) are shown for the circular force model
at $\alpha = 0$. In table I internal drag obtained from the circular force
model is compared with internal drag calculated from pressure survey
measurements using several methods of data reduction (described in the
Discussion Section) for $M_\infty = 4.06$, $\alpha = 0$.

DISCUSSION

General Flow Characteristics

Data for the circular and square ducts shown in figure 8 indicate essentially symmetrical flow about the duct longitudinal center line (vertical, 45° and horizontal axes) for the circular duct and vertical and horizontal for the square duct. Later in this report it will be demonstrated that this uniformity makes the accurate determination of exit momentum relatively straightforward for the circular ducts. However, for the square duct the flow characteristics are not completely defined in the duct corners which makes the determination of the exit momentum less accurate than for the circular ducts. For the models with a rectangular or a two-dimensional inlet, lack of flow symmetry near the exit is quite pronounced as seen in figures 9, 10(c), and 10(d). This characteristic greatly complicates the determination of exit momentum because much more detailed pressure measurements are required to adequately define the flow. Since static pressures from the duct-wall orifices (see Tests) and from the static-pressure probe near the wall were found to be in good agreement, data from the wall orifices are not presented in this report.

Determination of momentum near the exit of the ducts may be further complicated by changes in angle of attack as illustrated in figure 10. Flow characteristics for the models are shown along vertical and horizontal axes at $\alpha = 0$ and 5°. Flow distortion for the circular and square ducts is considerably greater at $\alpha = 5°$ than at $\alpha = 0$, particularly along the vertical axis (figs. 10(a) and (b)). The flow is no longer symmetrical about the duct longitudinal center line even at this relatively low angle of attack and accurate determination of momentum requires detailed pressure surveys. Pronounced changes in pressure distribution across the duct are also found for the models with rectangular and two-dimensional inlets at $\alpha = 5°$ (fig. 10(c) and (d)). At $\alpha = 0$ the static-pressure distributions across the duct are seen to be nearly constant for these models. However, at $\alpha = 5°$ these static-pressure distributions are considerably distorted along the horizontal as well as the vertical axes.

Effects of Internal Geometry

Effects on flow distortion that can be generated by variations in internal geometry, such as transition from rectangular to a circular section, are illustrated in figure 11. Shown in this figure are distributions of static-pressure ratio and Mach number across the exit for the 2-D inlet duct. The length of the rectangular-to-circular transition section has been systematically varied for these models.

It can be seen that flow distortion near the exit decreases as the transition section length increases from 3.5 to 5.5 inches and the length of the constant diameter section decreases from 6.0 inches to 4.0 inches. The measured static pressure-ratio distribution along the horizontal axis of the model with the longest transition section is noticeably improved (nearly constant), and the distribution along the vertical axis, is about the same as the other two models; for this configuration, the duct-exit Mach-number distribution tends more toward pipe flow and symmetry about the duct longitudinal center line. These results suggest that by properly proportioning the length of the transition section some reduction in flow distortion may be achieved.

Internal Drag From Force Measurements

As a basis for correlation with the pressure survey results, the drag coefficient for the internal sleeve of the force model circular duct was determined from the forces measured by strain-gage-instrumented flexures supporting the internal sleeve. The internal-drag coefficient, equal to .0975 C_{D_F} (shown in Table I), is an average of all force results obtained in this investigation at $M_\infty = 4.06$, $\alpha = 0$. Results obtained from repeat tests were found to vary by as much as ± 4 percent (approximately $\pm .0040 C_{D_F}$) at $\alpha = 0$ even though the test conditions, indicated by wind tunnel instrumentation, were duplicated in every detail as nearly as possible. Repeated measurements during any given run agreed within ± 1 percent. Furthermore, these measured variations were always verified when simultaneous pressure data were obtained. It would appear then that the $\pm 4\%$ variation is a characteristic peculiar to the wind tunnel and duct flow for each run.

Internal Drag From Pressure Surveys

An examination of figures 8, 13, and 14 for the circular ducts at $\alpha = 0$ shows the variation of static pressure p, total pressure p' and Mach number M to be relatively smooth near the exit. Even so, it may be shown that a wide range of internal-drag coefficient is obtained from a given set of data depending upon the analysis procedure applied to these data. Several data analysis procedures have been examined for the following purposes: (a) to determine the detail required of the pressure survey to adequately define the exit flow characteristics; (b) to show the sensitivity of the accuracy of the final results to the detail with which critical pressure regions in the flow are measured; and (c) to illustrate the utilization of experimental data by various data-reduction techniques. Results of this study are summarized in Table I.

The equation for internal-drag coefficient customarily derived

from momentum relationships (such as in ref. 1) can be written for $\alpha = 0$ and full capture mass flow ($\frac{m}{m_\infty} = 1.0$) as:

$$C_D = 2 + \frac{2}{1.4M_\infty^2} \left[1 - \left(\frac{\bar{p}}{p_\infty}\right) \left(1 + 1.4\bar{M}^2\right)\right] \tag{2}$$

where C_D is based on A_c.

If static- and total-pressure distributions across the duct exit are constant (as in a streamtube) with straight parallel streamlines then a single measurement of static pressure and a single measurement of total pressure could provide internal drag of the duct using equation 2. However, the assumption of a uniform flow is not generally realistic for viscous flows in ducts and, consequently, cannot be relied upon to provide a realistic calculation of internal drag. An examination of figures 8(a) and (b) shows that the exit distributions of pressures and Mach number are far from constant for even the circular-duct models. This indicates that it is difficult to define supersonic or hypersonic internal flow characteristics with any degree of reliability without a rather comprehensive flow survey.

Effects of Pressure-Measurement Errors

Errors in determining internal drag from experimental measurements are primarily from two sources: (1) inaccuracy in determining point values due to errors in measurement of static and/or total pressures and (2) inadequate determination of distributions of static and/or total pressures across the duct exit. To demonstrate effects of inaccuracies of measurement of static or total pressure on the calculation of internal drag, nominal conditions were assumed at the survey station which could give a value of internal drag equal to that obtained from force measurements ($C_{D_F} = .0975$, $p = .500$ psia, $\bar{M} = 3.015$) for $M_\infty = 4.06$ and $\alpha = 0$. Static or total pressures for the above exit conditions were then assumed to be in error by a fixed amount and internal drag was computed using these values in eq. 2.

The difference between the values of internal drag (computed from pressures) and internal drag obtained from force measurements ($C_{D_p} - C_{D_F}$) for ± 1, ± 2, or ± 3 percent error in either measured static or total pressure are shown, in figure 15. Exit Mach numbers $\bar{M}$ calculated from incorrect pressures are also shown in figure 15 for each computed condition.

Effect of errors in static-pressure measurements on measured internal drag is seen in figure 15 to be relatively insignificant for these conditions. With a 3 percent error in measurement of static pressure,

considered to be well within the accuracy of this investigation, the error in internal-drag coefficient is seen to be about .0020 or 2 percent C_{D_F}. This result also indicates that deviation from a straight line in static-pressure distribution across the duct of 3% or less will only slightly affect the results. Additional consideration of the effect of this error can be found in the Appendix.

Errors in total-pressure measurements are shown in figure 15 to have a considerable effect on internal drag results at these conditions. A 1% error in measurement of total pressure causes an error in internal-drag coefficient of nearly .0200 (about 20 percent of internal-drag coefficient determined from force measurements). The small amount of scatter in experimental results, however, indicates that total-pressure measurements were in error by less than one percent. For example, a ±0.2 percent error in total-pressure measurements causes an error in C_{D_P} approximately equal to that of C_{D_F} of ±4%. The large effect of errors in total-pressure measurements on the calculation of C_{D_P} in figure 15 points up the importance of a precise determination of total-pressure distribution at the survey station to obtain reliable internal drag from exit pressure measurements.

Comparison of Data-Analysis Procedures

Many fabrication and installation problems and the labor of obtaining data associated with an all-moveable survey mechanism, such as used in this investigation, can be reduced by using stationary pressure rakes. However, the number of probes which may be accommodated in a particular duct without adversely affecting the flow at the survey station must be considered. For the data analysis procedures to be demonstrated in this report it is assumed that a pressure rake could be designed with as many as ten static- and ten-total pressure probes which would adequately define the flow characteristics without affecting the flow. It is also assumed that such a rake will yield data consistent with results obtained using the traversing probe shown in figure 3 (i.e. negligible interference between probes).

For each of the procedures examined, the duct exit area was divided into several annuli. Each probe was hypothetically assumed to be positioned on the median radius of each annulus (one static and one total probe anywhere on the median radius) and includes a total-pressure probe on

the duct longitudinal center line and a static orifice in the duct wall
at the survey station (partial schematic shown in sketch 1).

Sketch 1
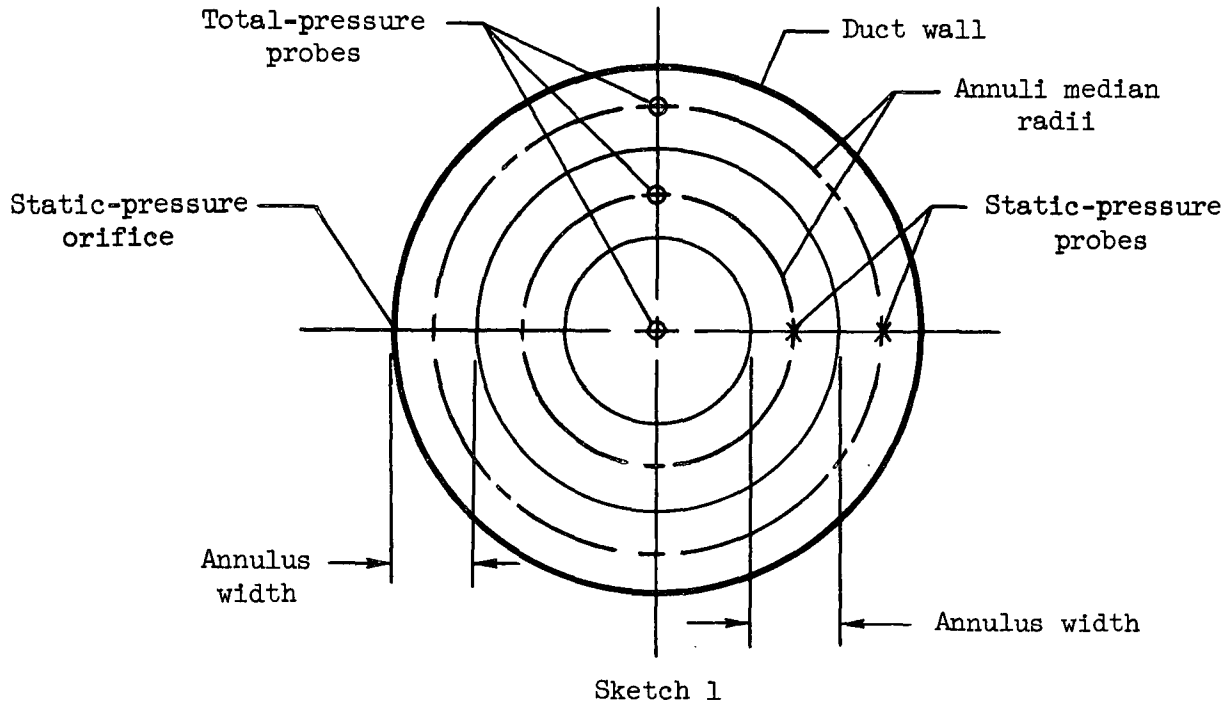
Pressures over a given annulus were assumed to be constant. Based upon
these assumptions, internal-drag coefficients were calculated for several
stationary rake arrangements and data analysis procedures as discussed
in the following paragraphs. The force measurements previously discussed
are used as a reference.

Procedure 1. - Internal skin friction drag was calculated for the
circular duct aligned with the flow (assuming no internal shock waves). The
duct was treated as a flat plate of span b equal to the circumference of
the duct and of length l equal to the length of the duct. Thickness of
the internal boundary layer was determined from Prandtl's Reynolds number
relationships for boundary-layer thickness on a flat plate. Defining
boundary-layer thickness δ as that at which the velocity is within one
percent of its asymptotic limit, for a laminar boundary layer

$$\frac{\delta_L}{x} = \frac{5}{R^{\frac{1}{2}}}$$

(5)

and for a turbulent boundary layer

$$\frac{\delta_T}{x} = \frac{.377}{R^{1/5}} \tag{6}$$

Boundary-layer thicknesses at the survey station determined from equations (5) and (6) are shown in figure 13(c). A comparison of the calculated boundary-layer thicknesses with the measured pressure data indicates that the internal boundary layer is essentially all-turbulent from duct inlet to exit. Internal-drag coefficient (skin-friction drag only since this is a straight constant area duct) computed for the all-turbulent condition using the method in Appendix A of reference 2. This procedure can be seen (Table 1) to give a result ($C_D = 0.0886$) that is approximately 11 percent below the reference internal-drag coefficient value.

Procedure 2a – The data analysis technique applied here was to divide the duct exit area into five annuli by dividing the duct radius into five equal increments ($\Delta r = r_{max}/ 5 = 0.1$ in.). Five static- and five total-pressure probes were assumed to be positioned on annuli median radii as previously described. These pressures were weighted according to the percentage of the total area over which the probe defined the pressure (area-weighted) and then the average values were computed from

$$\bar{p} = \Sigma_0^n \frac{p_n}{n} \tag{7}$$

$$\bar{p}' = \Sigma_0^n \frac{p'_n}{n} \tag{8}$$

Resulting C_D computed from these average values and equation (2) is shown in Table 1 to be less than half of the average value obtained from force measurements. Since equation (2) is relatively insensitive to errors in static pressure (see fig. 15) the lack of agreement is primarily due to the inaccuracy in the average total pressure $\bar{p}'$ that is derived from this method.

Procedure 2b – Here Procedure 2a is repeated for an assumed stationary rake with ten static- and ten total-pressure probes which are area-weighted and then averaged. C_D obtained from this procedure is shown in Table I to be approximately one-third the value determined from force measurements. These results would indicate that this procedure gives a total pressure which is too high in comparison to the value needed for good agreement with the force result (see fig. 15). The final result appears to be highly

sensitive to the positioning of the annuli in relation to the regions where the gradients in total pressure are high, such as near the wall.

Procedure 3a — The mathematical area-weighting process of Procedure 2, may be accomplished by positioning each probe of the rake on the median radii of equal-area increments. Assuming this technique is used in the design of a stationary rake with five static- and five total-pressure probes, then following the computation methods of Procedure 2, a value of C_D is obtained that is about one-third greater than the result obtained from force measurements (see Table I). Hence, the resulting average total pressure from this procedure is apparently too low to provide agreement with the force results:

Procedure 3b — The technique followed in Procedure 3a was repeated assuming ten static- and ten total-pressure probes in the stationary rake. C_D from this procedure is shown in Table I to be nearly two-thirds greater than the result obtained from force measurements.[1] This would indicate the average total pressure obtained from this procedure is again too low.

Procedure 4 — In instances where several pressures are required to adequately identify the flow characteristics over a particular region, each pressure may be considered as representing conditions for a stream tube in the flow. Since the change in momentum in each streamtube is the internal drag of the streamtube, integrating these changes over the area of interest provides a measure of the internal drag.

From Appendix A of reference 1 internal drag D of a streamtube, aligned with the freestream ($\alpha = 0$) may be written in terms of momentum and pressure of the internal flow at the relevant flow station as

$$D = m_i V_\infty - \int_A \left(p - p_\infty + \rho V^2 \right) dA \tag{9}$$

By assuming $m_i = m = m_\infty$ and total temperature remains constant throughout the flow (a* then remains constant) we can write for each streamtube:

$$C_D = \frac{D}{q_\infty S} = \frac{1}{q_\infty S} \left[\int_A p \left(\gamma M^2 \left(\frac{V_\infty/a^*}{V/a^*} \right)^\nu - \left(1 + \gamma M^2 \right) \right) dA + p_\infty A \right] \tag{10}$$

---

[1] This discrepancy, which is greater for procedure 3b than for 3a where fewer probes were assumed, is apparently associated with the sensitivity of the area-weighting analysis and is not completely understood.

This computational procedure was applied to the data obtained from the detailed pressure survey shown in figure 8(a) for the circular duct force model. The internal-drag coefficient computed in this manner (using all the measured pressures) is seen in Table 1 to agree exactly with the force measurement for this model. Comparison of the results using this streamtube analysis method with the preceding methods involving the determination of an average effective pressure are included in Table I. For these comparisons the internal-drag coefficient was computed using this computational method for the stationary rake geometries described in Procedures 2 and 3 (stationary rakes with either 5 or 10 static- and total-pressure probes). That is, each probe was considered to represent conditions for streamtubes contained in that particular annulus, and it was assumed that conditions over each annulus were constant. Differential area dA in equation (10) was equal to the area of the annulus represented by each individual probe.

Procedure 5 - It may be noted from figures 8, 13, and 14 that the distribution of static-pressure determined from the detailed survey for the circular duct is nearly linear from the center to the wall of the duct. Similarly, total-pressure distributions from the duct center to approximately $\frac{r}{d} = \pm 0.3$ and from $\frac{r}{d} = \pm 0.3$ to the duct wall are nearly linear and may be approximated by straight-line segments. Assuming pressure distributions to be symmetrical about the duct longitudinal center line, equations for straight-line segments, and hence equations which approximate pressure distributions, may be written if two values anywhere along the line segments are known. For example, two total pressures between $\frac{r}{d} = 0$ and say $\frac{r}{d} = .25$ (outside the boundary layer) would be required for one line segment and two total pressures between $\frac{r}{d} = .35$ and $\frac{r_{max}}{d} = 0.5$ (inside the boundary layer) would be required for the other line segment. Since static pressure at the duct wall is equal to total pressure at the wall, as few as three total-pressure probes, one static-pressure probe and a static-pressure orifice in the duct wall would provide sufficient data to approximate static and total pressure at any point across the circular duct in the survey plane. This procedure was applied to experimental pressure data obtained in this investigation for the circular duct at $M_\infty = 4.06$ and $\alpha = 0$. Static and total pressures were computed for ten equal-area annuli and internal drag computed using equation (10). The result, shown in Table I, is in good agreement with the result obtained from force measurements. The C_D value shown is an average value from several runs which includes the $\pm 4\%$ scatter as previously discussed, but for any given run, results from simultaneous force and pressure measurements agreed within ± 1 percent. A sample calculation, including equations used in this procedure, is presented in the Appendix of this report.

Effects of Mach Number

Effects of Mach number on the internal-drag coefficient obtained from force measurements are shown in figure 12 for Mach numbers between 3.7 and 4.4 for angles of attack of 0 and 5°. An estimate of the skin friction on the internal surface of the model over this Mach number range was made as described previously and is also shown in this figure. The difference in drag coefficient level (average of about 11 percent for $\alpha = 0$) between force measurements and skin friction calculations may be attributable at least in part to the fact that the calculations account only for friction losses and do not consider possible shock loss effects on the internal surfaces of the model. The experimental force data generally follow the trends indicated by skin friction estimates over this Mach number range at $\alpha = 0$. Increasing angle of attack from 0 to 5 degrees increased the measured internal drag approximately 16 percent. Some indication as to the reason for this drag increase can be seen in the results of figure 10(a). A marked increase in flow distortion is shown when angle of attack is increased from 0 to 5 degrees at $M_\infty = 4.06$ and is indicative of an increase in drag.

The computed internal-drag coefficients C_D shown in figure 12 were obtained from the data from figure 14.[2] Procedure 5, described in detail in the Appendix of this report and procedure 4 were followed for these computations. Differences between the computed values for procedure 5 and force measurements (as much as 11.25% at $M = 3.90$) are due, at least in part, to the inadequacy of the linear approximations of procedure 5 to predict the static- and total-pressure distributions as shown in figures 13 and 14. Even so, these results are generally in better agreement with the force measurements than are the skin-friction results. It can be reasoned that procedure 4 should agree better with the force measurements since the pressures are surveyed in greater detail. However, this was not the case when 3 axes were included in the calculations as indicated in the figure, or even with 6 axes as shown for Mach number 4.37. These results would seem to indicate the relatively great sensitivity of the calculations of C_D to the selected procedure.

When comparing the drag results obtained from force measurements at $\alpha = 0$ in figure 12 with the computed results from the pressure measurements of figure 14 (procedures 5, and 4, $\alpha = 0$), it is important to note that these measurements were not made simultaneously. Differences in these results (as at $M_\infty = 3.9$) are of the same order as those found from run to run ($\pm 4\%$) as previously discussed. Then these differences between force measurements and computed results from pressure measurements may only indicate changes in flow conditions in the duct from run to run due to varying airstream flow conditions in the wind tunnel.

---

[2]Attempts to calculate the internal drag of the circular duct model at $\alpha = 5$ degrees, using the methods demonstrated in this report, were unsuccessful due to the flow distortion and lack of detail in the flow surveys. This was also the case for the other models of this investigation at $\alpha = 0$ and 5 degrees (see fig. 10). Therefore, no results are presented for these cases.

Mach number effects on the static- and total-pressure distributions across the circular duct are shown in figures 13 and 14 for α = 0. Other than the expected differences in magnitude, (see fig. 14(a)), the distributions of total pressure p' from the duct longitudinal center line to the wall generally follow the same trends for each of the test Mach numbers. Inflections noted in the distribution of the measured static pressure p (fig. 14(b) at lower Mach numbers tend to dissipate with increasing Mach number.

CONCLUSIONS

Flow characteristics near the exit of several small scale ducts, designed to simulate the external aerodynamics of nacelles of airbreathing propulsion units, have been studied in the wind tunnel at Mach numbers from 3.7 to 4.4 for angles of attack of 0 and 5 degrees. From this study the following conclusions have been drawn:

1. For a constant diameter straight circular duct with free stream flow at the inlet and a supersonic exit:

    (a) Flow near the exit is symmetrical about the duct longitudinal center line at α = 0 degrees but considerably distorted at α = 5 degrees.

    (b) Area weighting and averaging of static and total pressures measured at either five or ten equal increments across the duct near the exit provides a measurement of internal drag of the duct at α = 0 which does not agree well with results obtained from force measurements.

    (c) An arithmetic average of either five or ten static- and total-pressure measurements, obtained for equal increments of the exit area, provides internal drag results for this duct at α = 0 which do not agree well with results from force measurements.

    (d) Integration of internal drag of streamtubes within the duct (either five or ten of equal area), as determined from static and total pressures measured at the median radius of each streamtube, provides an internal drag for this duct at α = 0 which is in good agreement with results from force measurements.

    (e) Flow characteristics near the exit of this duct at α = 0 may be identified by as few as three total-pressure probes, one static-pressure probe and a duct-wall static orifice, if they are carefully located. Internal drag of this duct at α = 0 may be computed from a method demonstrated in

this report and will be in good agreement with results from force measurements obtained simultaneously.

(f) Irregularities in static- and total-pressure distributions across the duct decrease with increasing free stream Mach number at $\alpha = 0$.

(g) A reasonable estimate of internal drag of the duct can be made at $\alpha = 0$ based on boundary-layer theory for a flat plate provided the boundary layer conditions inside the duct can be determined.

2. For all configurations of this investigation:

(a) Neither static- nor total-pressure is constant across the duct at $\alpha = 0$ or 5 degrees.

(b) Detailed static- and total-pressure measurements near the duct exit are required to define the flow characteristics through the duct to determine internal drag of the duct with any reasonable accuracy.

(c) Internal drag results obtained from pressure surveys are very sensitive to errors in total-pressure measurements and rather insensitive to errors in static-pressure measurements.

(d) Flow characteristics near the duct exit show a pronounced change for a 5 degree change in angle of attack.

(e) Flow distortion near the exit of the ducts is sufficient at $\alpha = 5$ degrees to require considerably more detailed pressure surveys than at $\alpha = 0$ to accurately assess momentum at the exit.

APPENDIX

In Procedure 5 of the Discussion, a method was described for calculating the internal drag of a circular duct. The procedure was based upon the use of a minimum number of orifices discretely located in the duct exit region. The purpose in this Appendix is to demonstrate the method by showing the details of the computations used therein. A comparison will be made between results obtained from this approximate procedure and from force measurements. Pressure measurements used in these calculations and force measurements were made simultaneously.

Internal drag of the circular duct at $\alpha = 0$ will be calculated using a portion of the experimental data presented in figure 13(c). These static- and total pressure distribution curves will be approximated assuming a stationary rake with a geometry which places total-pressure probes at $r = 0$, $\dfrac{r_{max}}{3}$, and $\dfrac{2r_{max}}{3}$. Static pressures will be assumed to be at $\dfrac{r_{max}}{3}$, and also at the duct wall where static and total pressures are equal. The assumed placement of probes was determined from knowledge gained from calculation of boundary layer characteristics at the survey station as shown in figure 13(c). For this example 10 equal area annuli (streamtubes) will be considered. Since each annulus is considered as a streamtube, the conditions at the center line or mean radius of the annulus must be defined. Accordingly, the area and mean radius for any annulus in the survey plane is defined as follows:

$$A_N = A_n = \frac{A_{total}}{N} = Ct \quad \text{(see sketch A-1)} \quad \text{(A1)}$$

where

A_n = area of annulus

A_{total} = duct exit area

N = total number of annuli being considered

C = circumference of annulus n at the median radius

t = thickness of annulus n
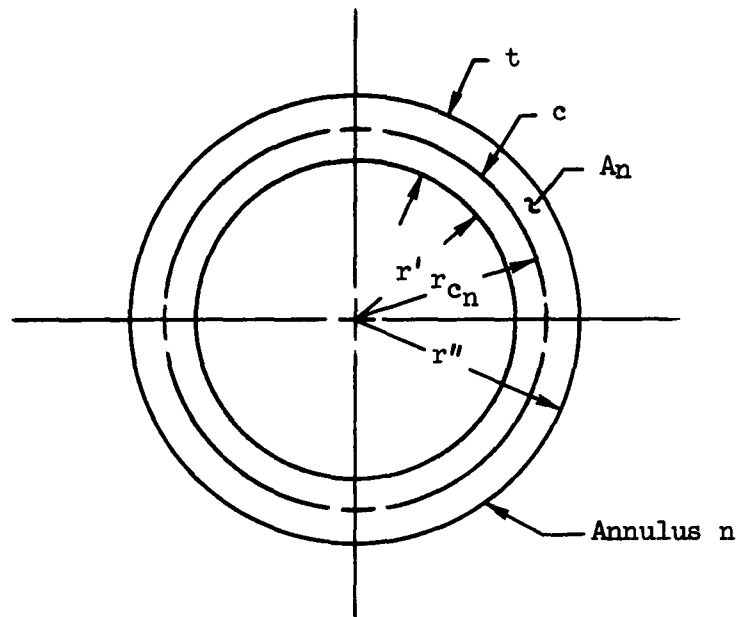
Sketch A-1

The median circumference of annulus n is

$$C = 2\pi\ r_{c_n} \tag{A2}$$

r_{c_n} = median radius of annulus n.

and the thickness of annulus n is

$$t = r'' - r' \tag{A3}$$

r'' = outer radius of annulus n

r' = inner radius of annulus n
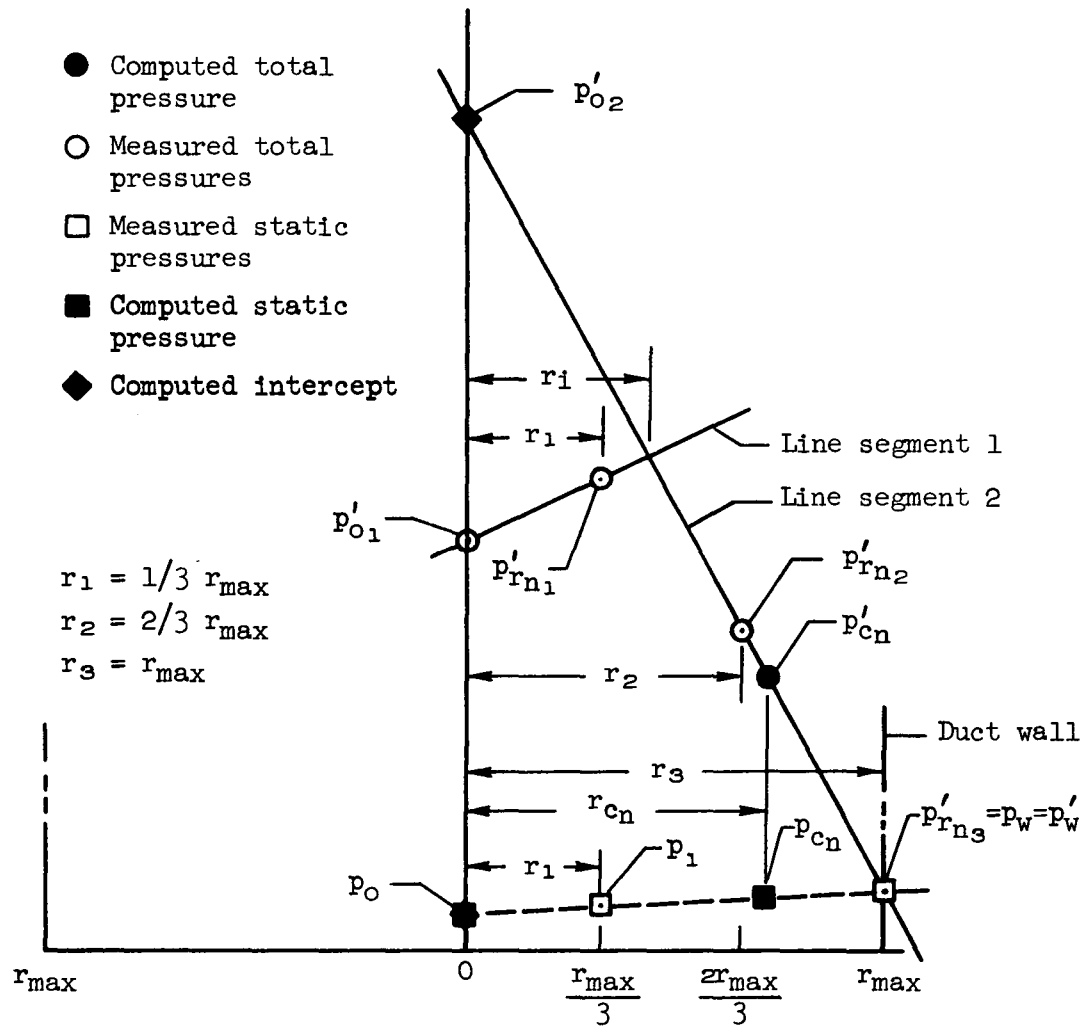
Sketch A-2

The median radius of annulus n is

$$r_{c_n} = r' + \left(\frac{r'' - r'}{2}\right) \tag{A4}$$

Combining (A1), (A2), (A3) and (A4) we have

$$A_n = 2\pi r_{c_n} t = \text{constant}$$

$$A_n = 2\pi \left[r' + \left(\frac{r'' - r'}{2}\right)\right] \left(r'' - r'\right) \tag{A5}$$

Beginning with either the innermost annulus $r' = r_o = 0$, or with the outermost annulus $r'' = r_{max}$, the r_{c_n} for each annulus may be calculated.

Referring to sketch A-2 equations for line segments approximating static- and total-pressure distributions may be written in terms of experimentally determined pressures obtained from probes located as previously assumed. The equation for the line approximating static-pressure distribution is

$$p = m_s r + p_o \tag{A6}$$

where

   p = exit static pressure

   m_s = slope of the line representing static-pressure distribution

   r = radius to any point

   p_o = intercept = exit static pressure at the duct longitudinal
         center line ($r = 0$)

The slope of this line is

$$m_s = \frac{\left(p_w - p_1\right)}{\left(r_{max} - r_1\right)} \tag{A7}$$

   p_w = static pressure at the duct wall

   p_1 = static pressure at r_1

Combining (A6) and (A7)

$$p = \left(\frac{p_w - p_1}{r_{max} - r_1}\right) r + p_o \tag{A8}$$

To determine the intercept p_o

$$\left(\frac{P_w - P_1}{r_{max} - r_1}\right) = \frac{\left(P_w - P_o\right)}{r_{max}}$$

(A9)

$$P_o = P_w - r_{max}\left(\frac{P_w - P_1}{r_{max} - r_1}\right)$$

Combining (A8) and (A9)

$$p = \left(\frac{P_w - P_1}{r_{max} - r_1}\right)\left(r - r_{max}\right) + P_w$$

(A10)

Then static pressure at the median radius of each annulus is

$$P_{c_n} = \left(\frac{P_w - P_1}{r_{max} - r_1}\right)\left(r_{c_n} - r_{max}\right) + P_w$$

(A11)

The procedure used for determining equations which approximate static pressures may also be used for total pressures. As previously discussed, total-pressure distribution is approximated by two straight line segments and, therefore, equations for each line segment are required (sketch A-2). Let

p'_{o_1} = total pressure at the duct center line $r = 0$ (intercept) for line segment 1

p'_{o_2} = total pressure at the duct center line $r = 0$ (intercept) for line segment 2.

$p'_{r_{n_1}}$ = total pressure at r_1 on line segment 1

$p'_{r_{n_2}}$ = total pressure at r_2 on line segment 2

$p'_{r_{n_3}}$ = total pressure at $r_3 = r_{max}$ on line segment 2

r_1 = radius to the intersection of line segments 1 and 2

The equation for pressure at any point in line segment 1 (Sketch A-2) may be written as

$$p'_{r_n} = m_1 \, r_{1_n} + p'_{o_1} \tag{A12}$$

p'_{r_n} = exit total pressure at r_{1_n} on line segment 1

m_1 = slope of line segment 1

r_{1_n} = radius to any point on line segment 1

p'_{o_1} = total pressure on the duct center line (r = 0) for line segment 1

The slope of this line segment is

$$m_1 = \frac{p'_{r_{n_1}} - p'_{o_1}}{r_1 - r_o}, \quad r_o = 0 \tag{A13}$$

The value of p'_{o_1} is determined from experiment. Then combining (A12) and (A13)

$$p'_{r_n} = \left(\frac{p'_{r_{n_1}} - p'_{o_1}}{r_1} \right) r_{1_n} + p'_{o_1} \quad \text{for } r_{1_n} < r_1 \tag{A14}$$

Similarly for any point on segment 2

$$p'_{r_n} = m_2 \, r_{2_n} + p'_{o_2} \tag{A15}$$

p'_{r_n} = exit total pressure at r_{2_n} on line segment 2

m_2 = slope of line segment 2

r_{2_n} = radius to any point on line segment 2

p'_{o_2} = total pressure at the duct center line, r = 0 (intercept) for line segment 2

The slope of line segment 2 is

$$m_2 = \frac{p'_{r_{n_3}} - p'_{r_{n_2}}}{\left(r_{max} - r_2\right)} \tag{A16}$$

The intercept of line segment 2 is determined from

$$\frac{p'_w - p'_{r_{n_2}}}{r_{max} - r_2} = \frac{p'_w - p'_{o_2}}{r_{max} - r_o} = \frac{p'_w - p'_{o_2}}{r_{max}}$$

or

$$p'_{o_2} = p'_w - r_{max}\left(\frac{p'_w - p'_{r_{n_2}}}{r_{max} - r_2}\right) \tag{A17}$$

Combining equations (A15), (A16) and (A17)

$$p'_{r_n} = \left(\frac{p'_{r_{n_3}} - p'_{r_{n_2}}}{r_{max} - r_2}\right) r_n + p'_w - r_{max}\left(\frac{p'_w - p'_{r_{n_2}}}{r_{max} - r_2}\right) \tag{A18}$$

for $r_n > r_i$

    The intersection point of curves representing total-pressure distribution is required in order to select which equation to use in computing the total pressures for each annulus. (Equation (A14) for $r_i < r_i$ or equation (A18) for $r_2 > r_i$. At this intersection point r_i, equation (A14) and (A18) are equal. Then

$$p'_{r_1} = p'_{r_2} \quad \text{at } r_i \text{ and}$$

$$m_1 r_i + p'_{o_1} = m_2 r_i + p'_{o_2}$$

so

$$r_i = \frac{p'_{o_2} - p'_{o_1}}{m_1 - m_2} \tag{A19}$$

The final equation to compute total pressure at the median radius of each annulus (stream-tube) for line segment 1 ($r_c < r_i$) is

$$p'_{c_1} = \left(\frac{p'_{r_{n_1}} - p'_{o_1}}{r_1}\right) r_{c_n} + p'_{o_1} \tag{A20}$$

and for line segment 2 $(r_c > r_1)$ is

$$p'_{c_2} = \left(\frac{p'_{r_{n_3}} - p'_{r_{n_2}}}{r_{max} - r_2}\right) r_{c_n} + p'_w - r_{max}\left(\frac{p'_w - p'_{r_{n_2}}}{r_{max} - r_2}\right) \tag{A21}$$

With these equations a value for static and/or total pressure may be computed at any point across the duct in the survey plane assuming flow is symmetrical about the duct longitudinal center line.

Once static and total pressures have been determined at the median radius of each annulus in the survey plane, internal drag or change in momentum between the duct inlet and the survey plane may be determined for each streamtube. Inlet conditions are determined from free stream conditions and we proceed as in reference 1, Appendix A.

$$D = m_1 V_1 - \int_A (p - p_\infty + \rho V^2)\, dA \tag{A22}$$

for small angles of attack ($\alpha \to 0$).

For full capture at the inlet and no boundary layer bleed in the duct

$$m_1 = m_\infty = m = \int_A \rho\, V\, dA \tag{A23}$$

Combining equations (A22) and (A23) and noting $V_1 = V_\infty$

$$D = \int_A \rho V V_\infty dA - \int_A (p - p_\infty + \rho V^2)\, dA \tag{A24}$$

Since $\rho V^2 = \gamma p M^2$
equation (A24) can be written as

$$D = \int_A \left(\frac{\gamma p M^2}{V}\right) V_\infty dA - \int_A (p - p_\infty + \gamma p M^2)\, dA \tag{A25}$$

Regrouping:

$$D = \int_A p \left[\left(\gamma M^2 \frac{V_\infty}{V}\right) - \left(1 + \gamma M^2\right)\right] dA + \int_A p_\infty dA \tag{A26}$$

and $D = \int_A p \left[\left(\gamma M^2 \right) \frac{V_\infty}{V} - \left(1 + \gamma M^2 \right) \right] dA + p_\infty A$ (A27)

By assuming total temperature remains constant, the critical speed of sound a* remains constant.

Then

$$D = \int_A p \left[\gamma M^2 \left(\frac{V_\infty/a*}{V/a*} \right) - \left(1 + \gamma M^2 \right) \right] dA + p_\infty A \qquad (A28)$$

Letting $f(M') = \left[\gamma M^2 \left(\frac{V_\infty/a*}{V/a*} \right) - (1 + \gamma M^2) \right]$ (A29)

where $(V_\infty/a^*) = f(M_\infty)$ and $(V/a*) = f(M)$, (ref. 3). Now for annulus n

$$D = \int_A p \left[f(M')dA \right] + p_\infty A \qquad (A30)$$

M = duct exit Mach number = $f\left(p/p' \right)$

A = area

p = static pressure at the survey station for annulus n

p' = total pressure at the survey station for annulus n

γ = gas constant

Then for the complete duct

$$C_D = \frac{\sum_1^n D}{q_\infty S} \qquad (A31)$$

Inputs required for the computation and values used in this example of procedure 5 are as follows:

<u>Inputs</u>

(1)	M_∞	4.06
(2)	p_{t_∞}	49.12 psia
(3)	p_∞	0.299 psia
(4)	A	0.7854 wq. in.
(5)	A_i	0.7854 sq. in.

(6)   d   1.000 in.

(7) r_{max} 0.500 in.

(8) p'_{o_1} 8.15 psia

(9) p'_{o_2} 8.65 psia

(10) r_1 $\dfrac{r_{max}}{3} = 0.167$ in.

(11) p'_2 7.75 psia

(12) r_2 $\dfrac{2}{3} r_{max} = 0.333$ in.

(13) $p'_{r_{n_3}} = p'_w$ 0.540 psia

(14) r_3 0.500 in.

(15) p_1 0.497 psia

(16) p_w 0.540 psia

(17) N   10

(18) q_∞ $\dfrac{\gamma \, p_\infty \, M_\infty^2}{2}$

(19) S   0.7854 sq. in.

(20) γ 1.4 for air

Steps in the computation are as follows:

STEP	OPERATION	EQ. NO.
1	Compute A_n	(A1)
2	Compute r_{c_n}	(A4)
3	Compute m_s	(A7)
4	Compute p_o	(A9)
5	Compute p_{c_n}	(A11)
6	Compute m_1	(A13)
7	Compute m_2	(A16)

STEP	OPERATION	EQ. NO.
8	Compute p'_{o_2}	(A17)
9	Compute r_i	(A19)
10	Compute p'_{c_1} for $r_{c_n} < r_i$	(A20)
11	Compute p'_{c_2} for $r_{c_n} > r_i$	(A21)
12	Compute $f(M')$ where $M = f(p/p')$	(A30)
13	Compute D for each A_n	(A31)
14	Compute C_D	(A32)

The result from this computation for the cylindrical duct is $C_{D_i} = 0.0987$ which compares with a value of 0.0996 from force measurements obtained concurrently with the pressure data. These values differ slightly from those presented in Table I but are within the variations from run to run cited in the Discussion Section.

REFERENCES

1. Britton, J. W.: Measurement of the Internal Drag of Air Breathing Installations on Slender Wing-Body Combinations at Supersonic Speeds. British Technical Report No. 65274.

2. Hicks, Raymond M.; and Hopkins, Edward J.: Effects of Spanwise Variation of Leading-Edge Sweep on the Lift, Drag, and Pitching Moment of a Wing-Body Combination at Mach Numbers From 0.7 to 2.94. NASA TN D-2236, April 1964.

3. Ames Research Staff: Equations, Tables, and Charts for Compressible Flow. NACA Rep. 1135, 1953. (Supersedes NACA TN 1428)

TABLE I
CIRCULAR DUCT

$M_\infty = 4.06$, $\alpha = 0$

$P_{t_\infty} = 49.1$ psia

Reference internal-drag coefficient $C_{D_F} = .0975$

PROCEDURE	C_D		
1. Skin-Friction		.0886	
2a 5 Static- and 5 total-press. probes, equally spaced, area-weighted.	.0462		.1000
2b 10 static- and 10 total-press. probes, equally spaced, area-weighted.	.0311		.1238
3a 5 static- and 5 total-press. probes, equal-area spacing.	.1295	eq.(2)	.0907
3b 10 static- and 10 total-press. probes, equal-area spacing.	.1578		.0901
4 Detail pressure survey from traversing probe.			.0975
5. Approximation method, linearized pressure distribution.			.0987

eq.(10) brackets the right column (2a–5).

Square duct

Circular duct

2-D inlet duct

Rectangular inlet duct

Airflow
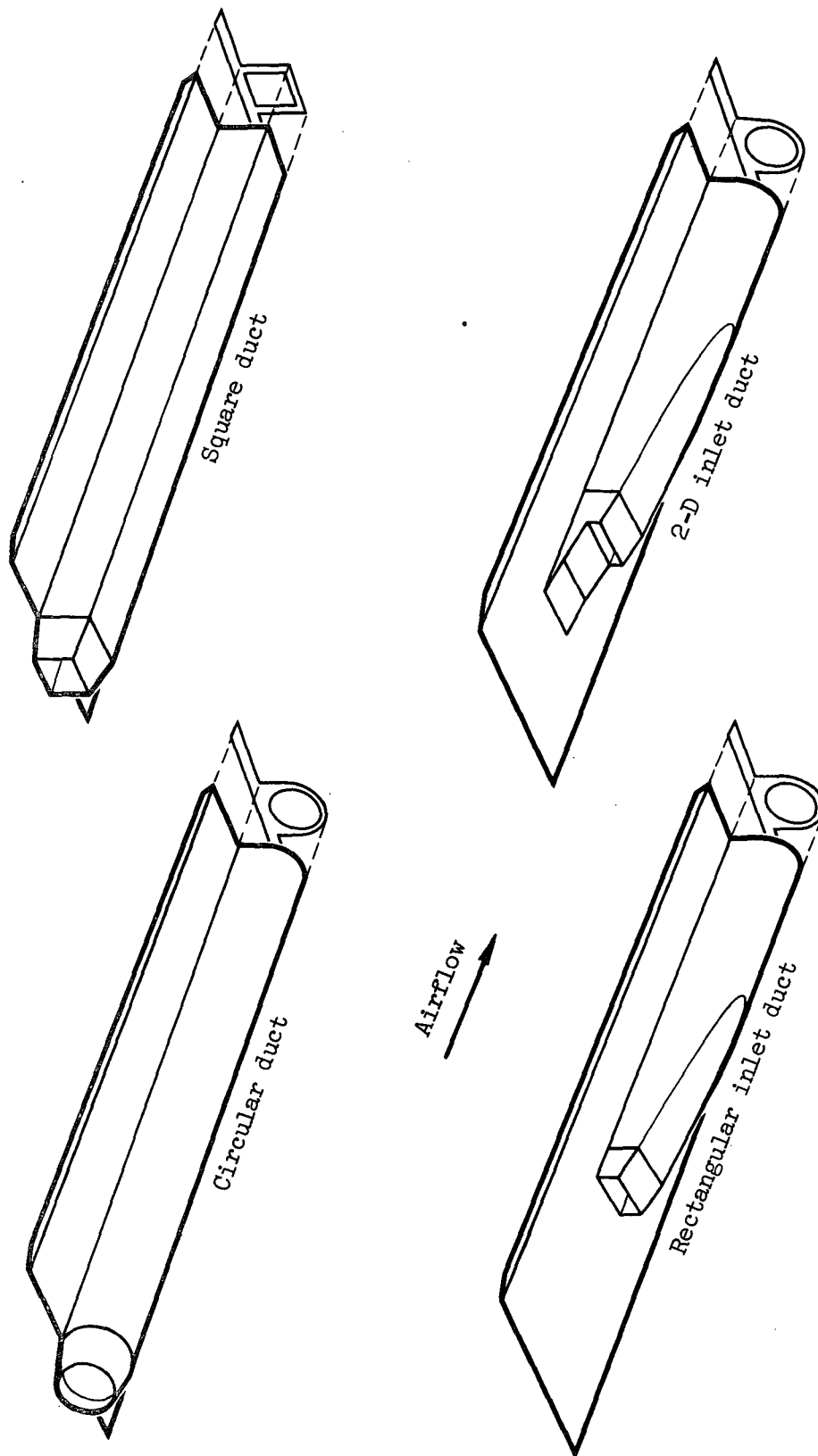
Figure 1.- Models.
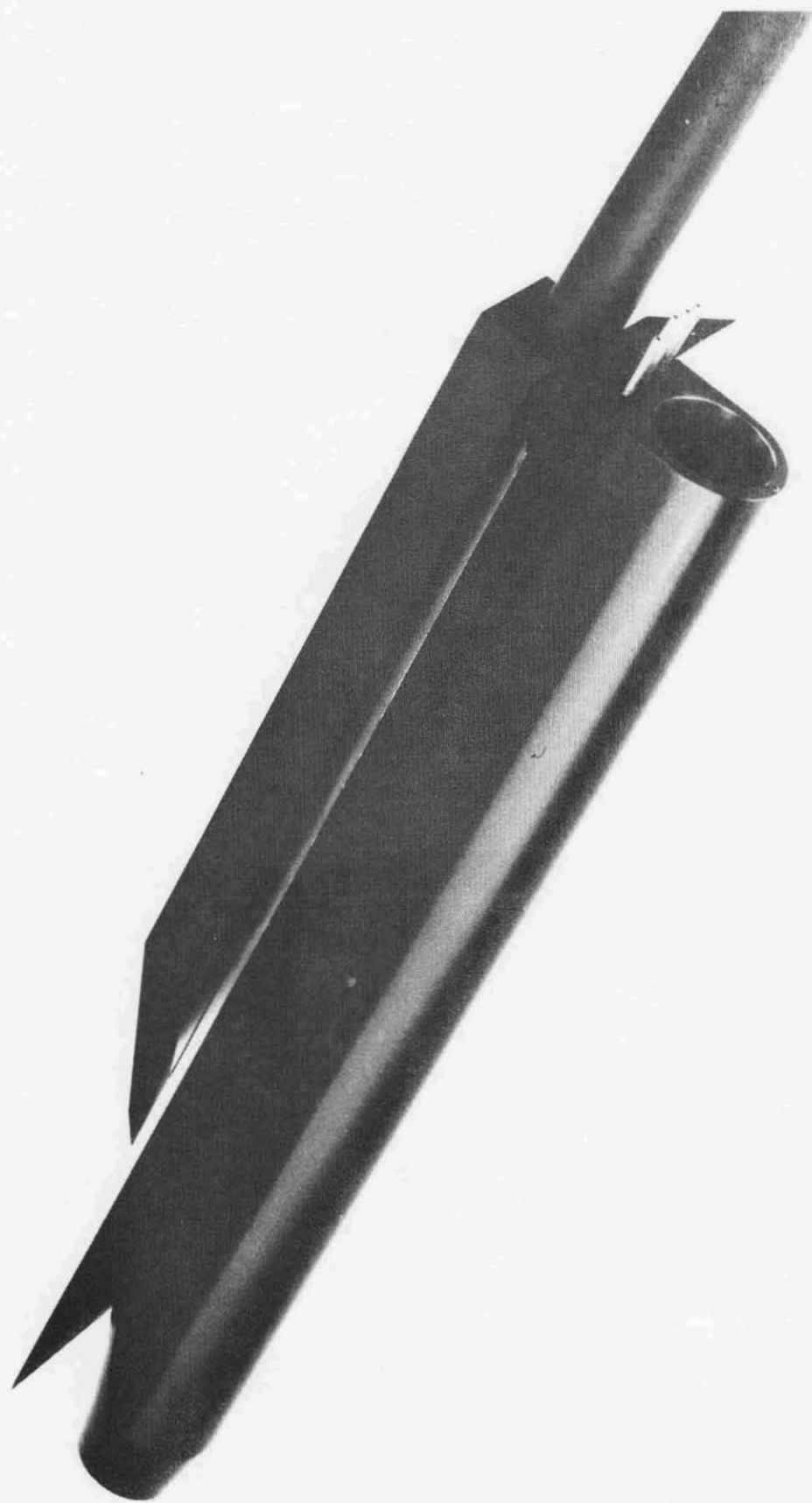
(a) Three-quarter rear view

Figure 2.- Circular duct model.
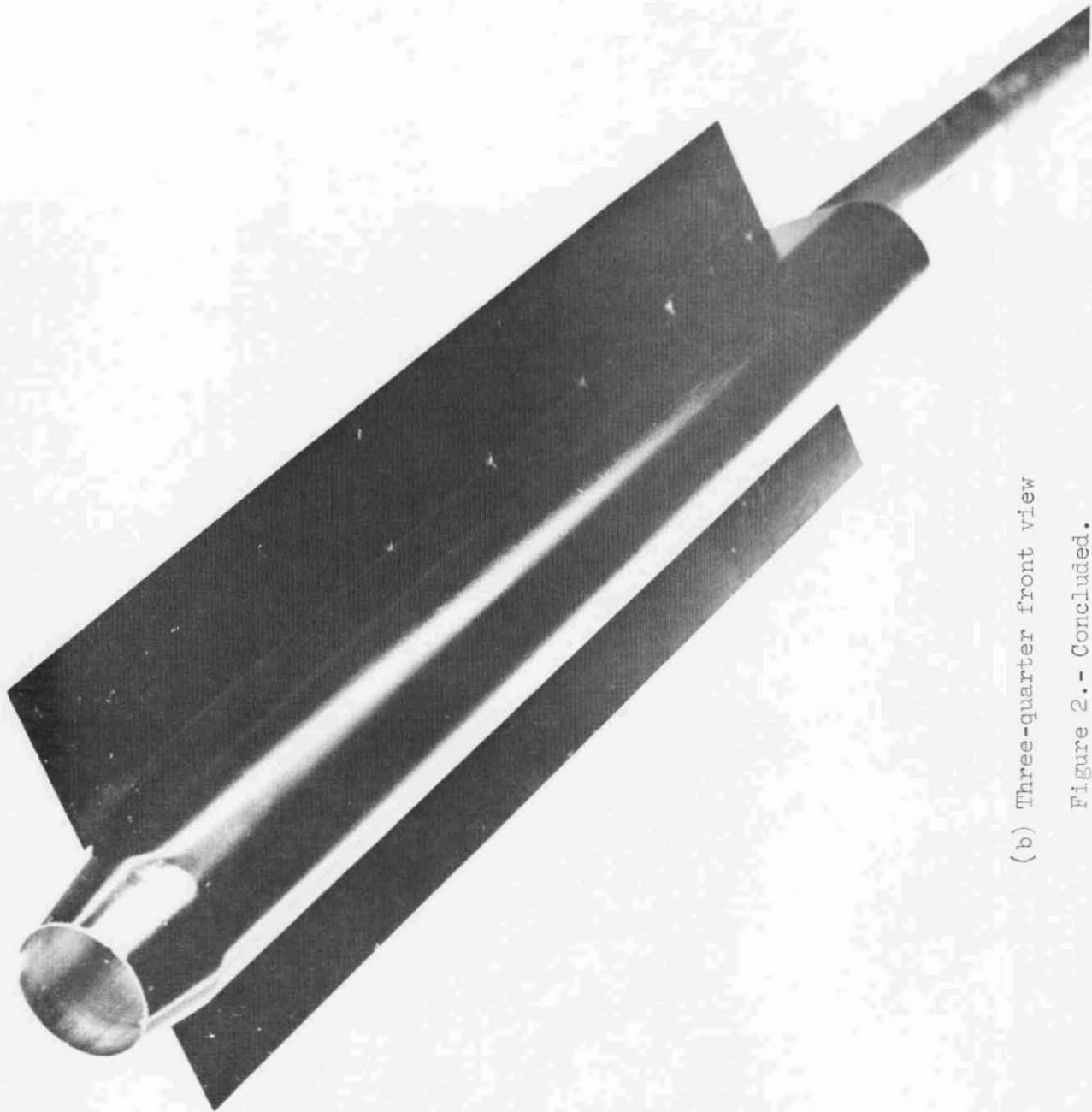
(b) Three-quarter front view

Figure 2.- Concluded.

Flexure–chamber
pressure tube

Base pressure
tube

Sting support

Flexible diaphragm

Rear flexure

Probe

Body

Front flexure

Inner sleeve

Duct outer wall

Wing
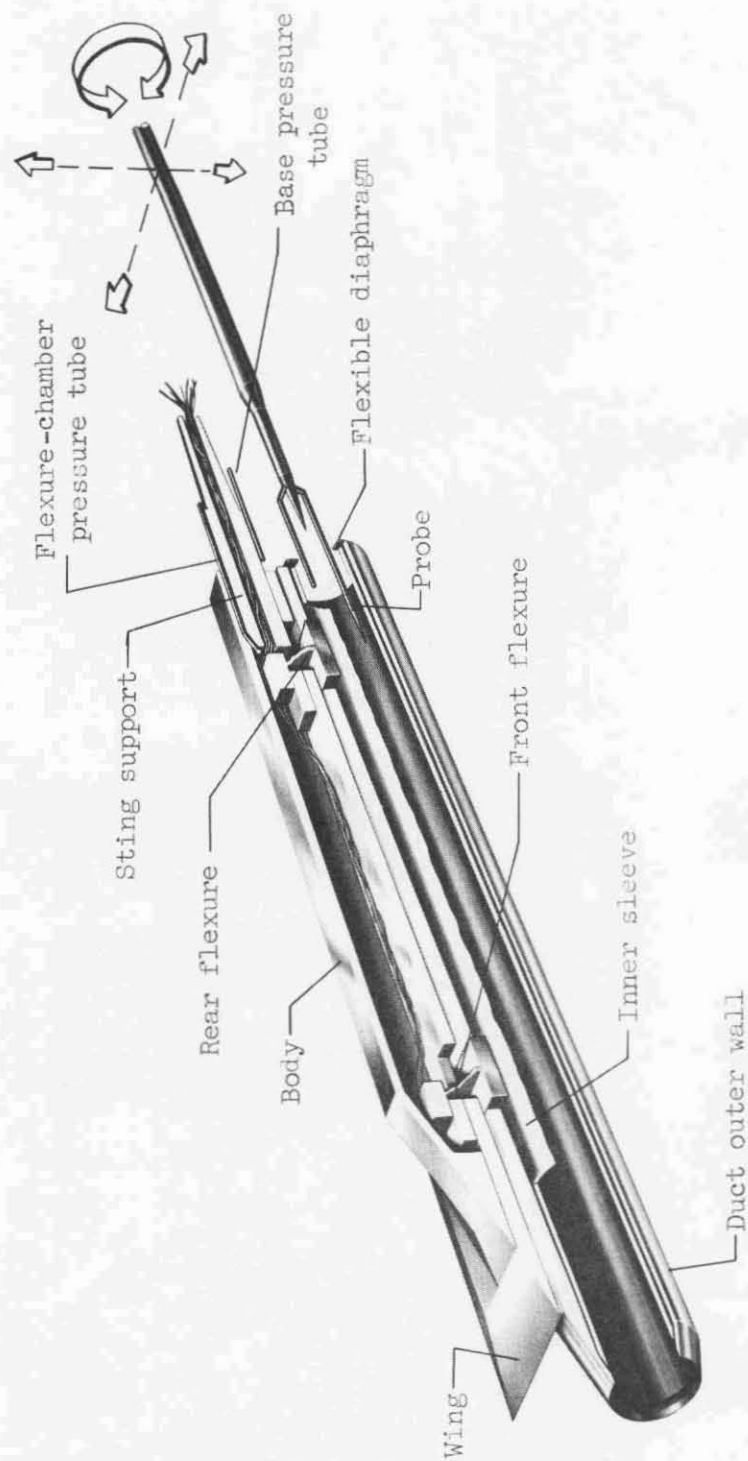
(a) Isometric sectional view

Figure 3.– Circular duct force model.

Thermocouple leads

Flexure-cavity
thermocouple

Strain-gauge leads

Flexible diaphragm

Inner sleeve

Wing

Rear flexure

Front flexure
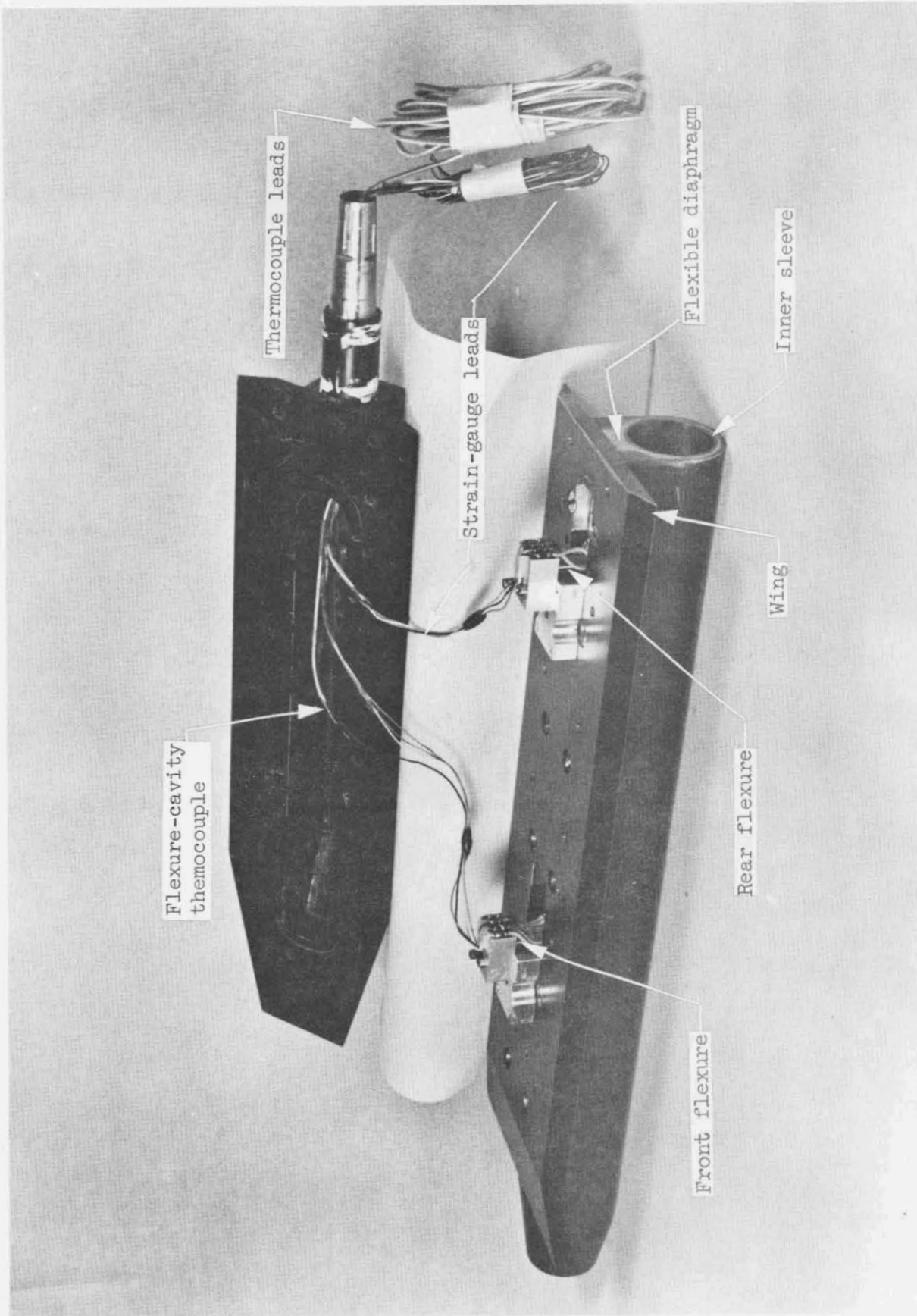
(b) Three-quarter rear view

Figure 3.- Continued.

3.34

1.25

Note: All dimensions
are in inches
except as noted

11.00

1.00 diam

12.41

10°

10°
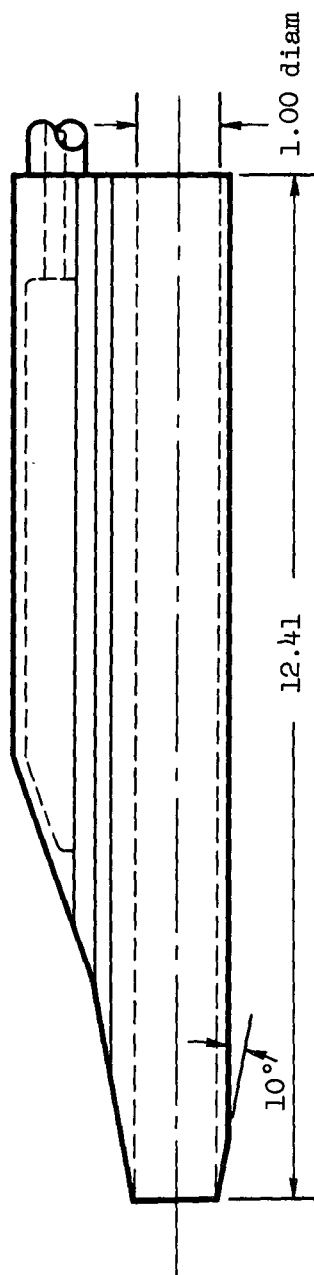
(c) Dimensions

Figure 3.- Concluded.
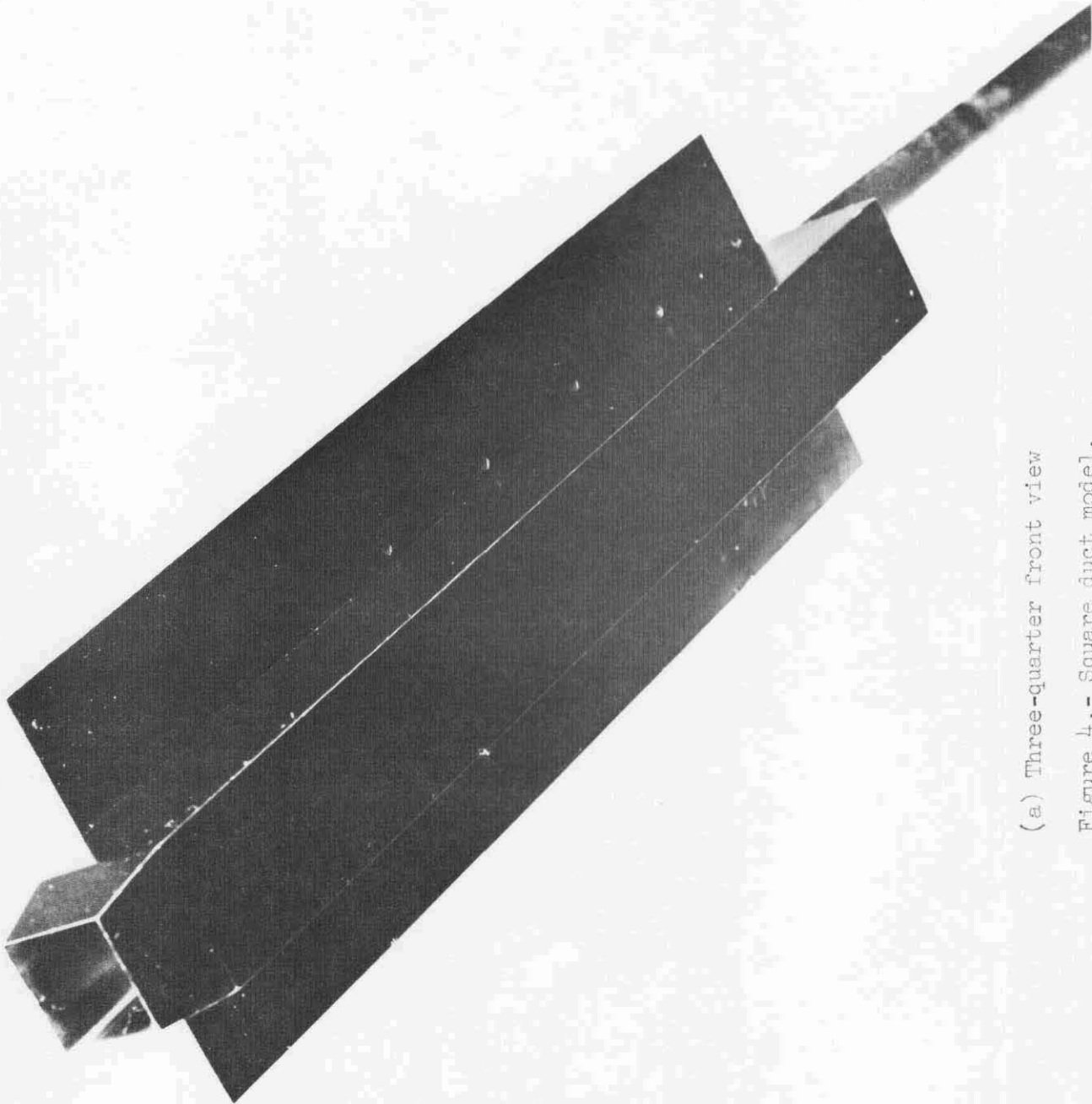
(a) Three-quarter front view

Figure 4.- Square duct model.
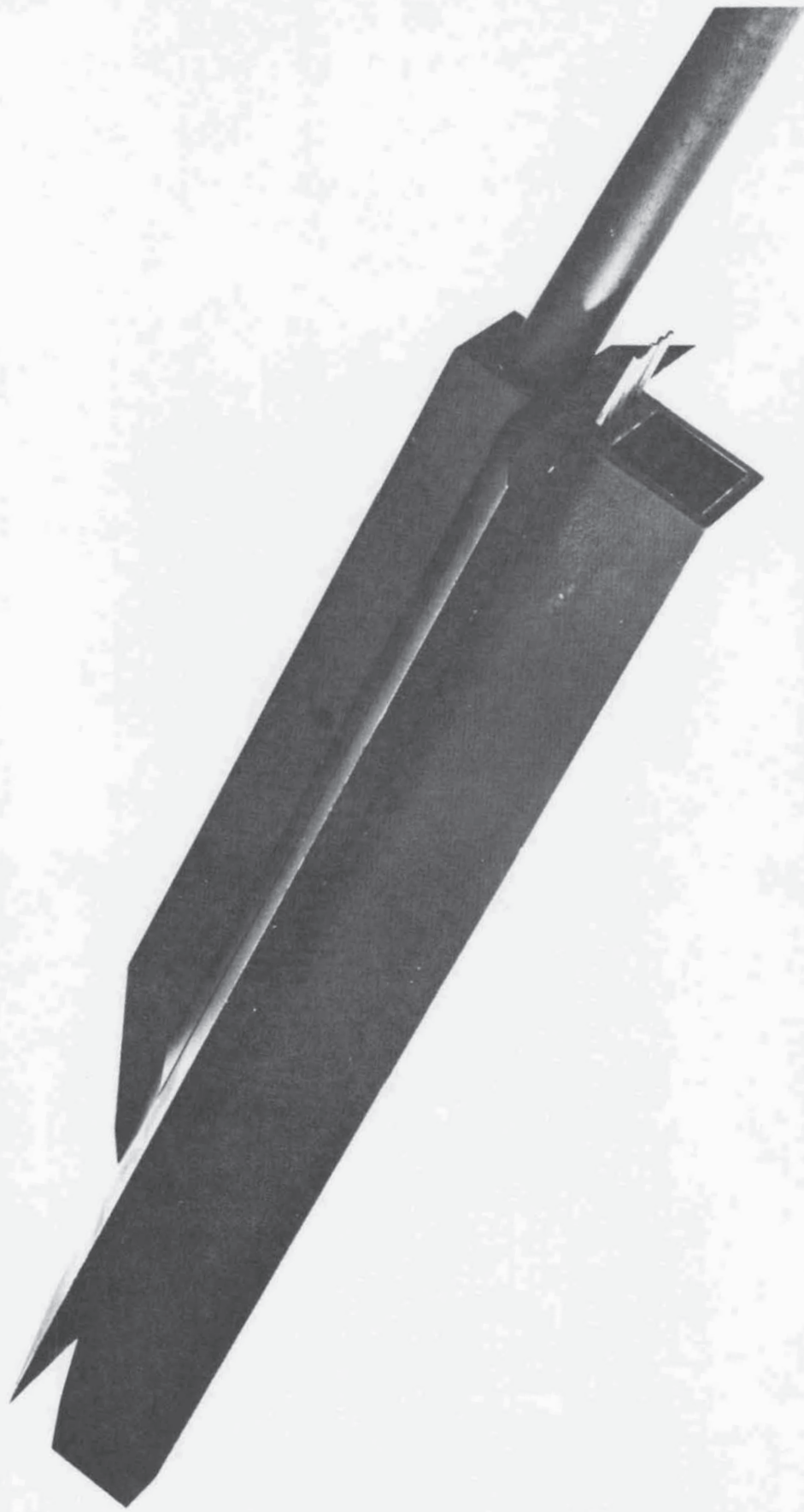
(b) Three-quarter rear view

Figure 4.- Concluded.
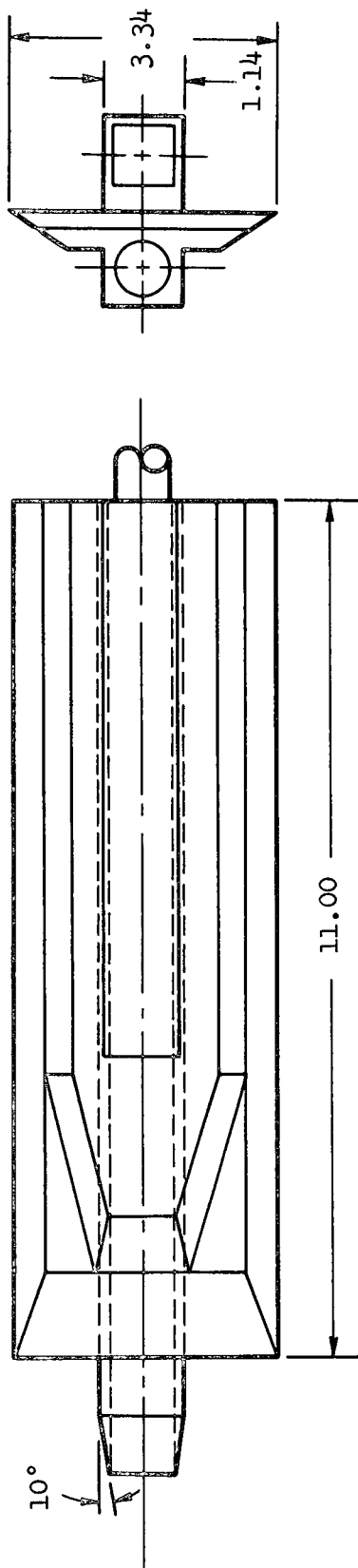
Note: All dimensions are in inches except as noted
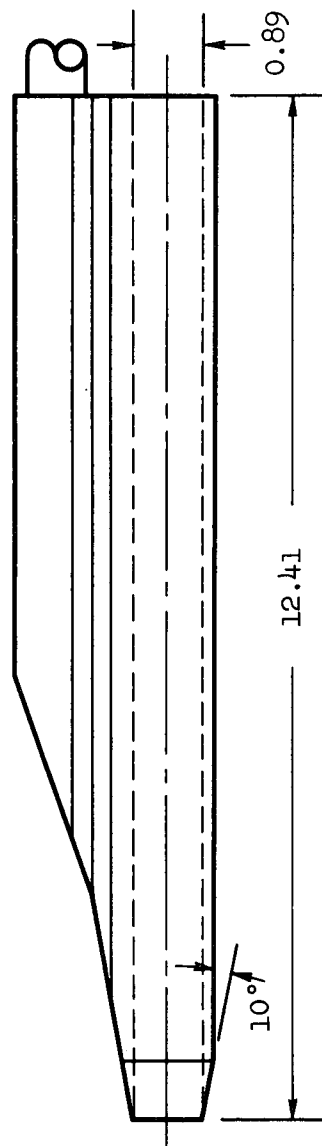
(c) Dimensions

Figure 4.- Concluded.
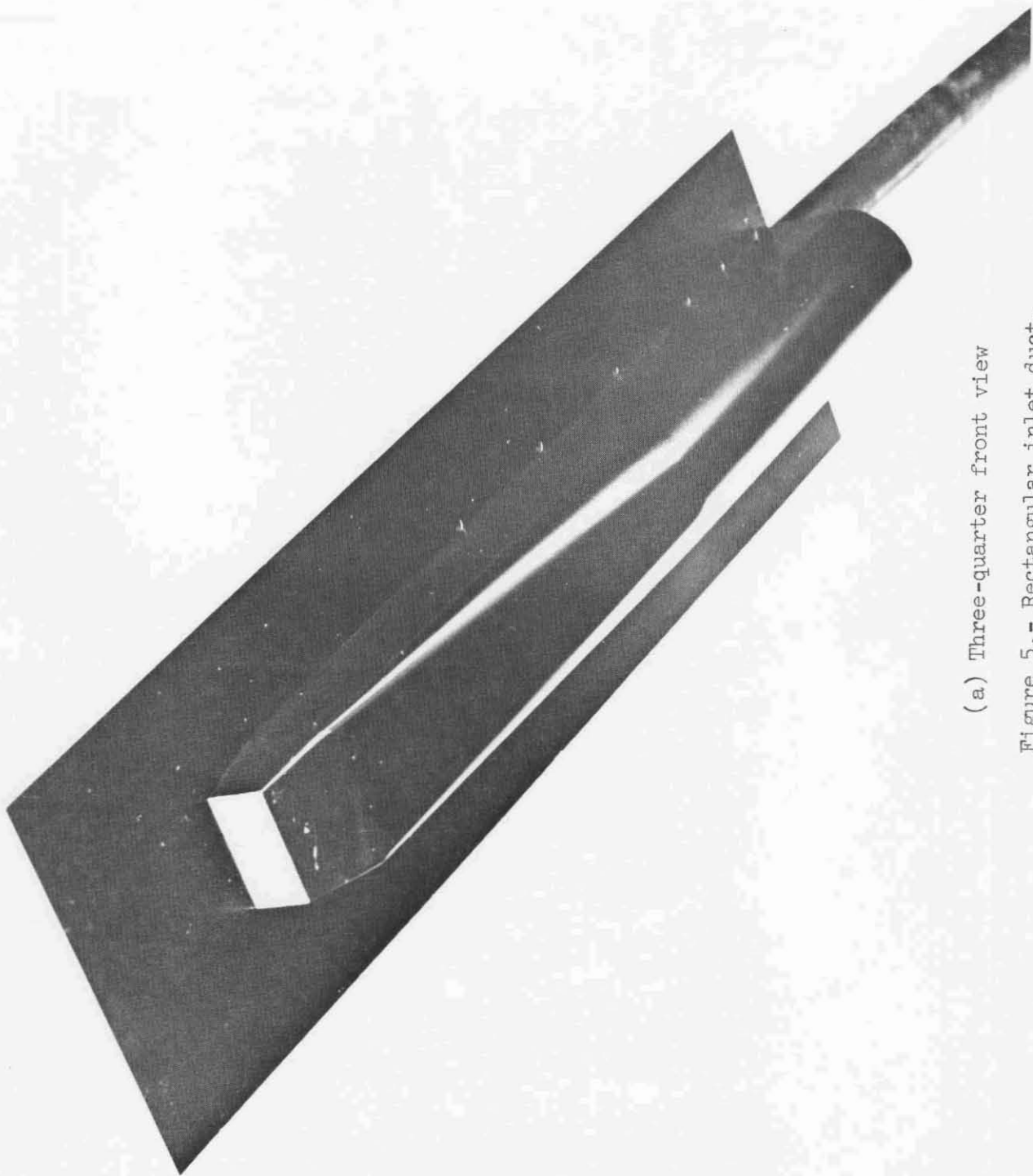
(a) Three-quarter front view

Figure 5.- Rectangular inlet duct.

3.34

1.25

Note: All dimensions
are in inches
except as noted

1.00 diam

Transition
4.6

1.4

11.00

13.17

10°
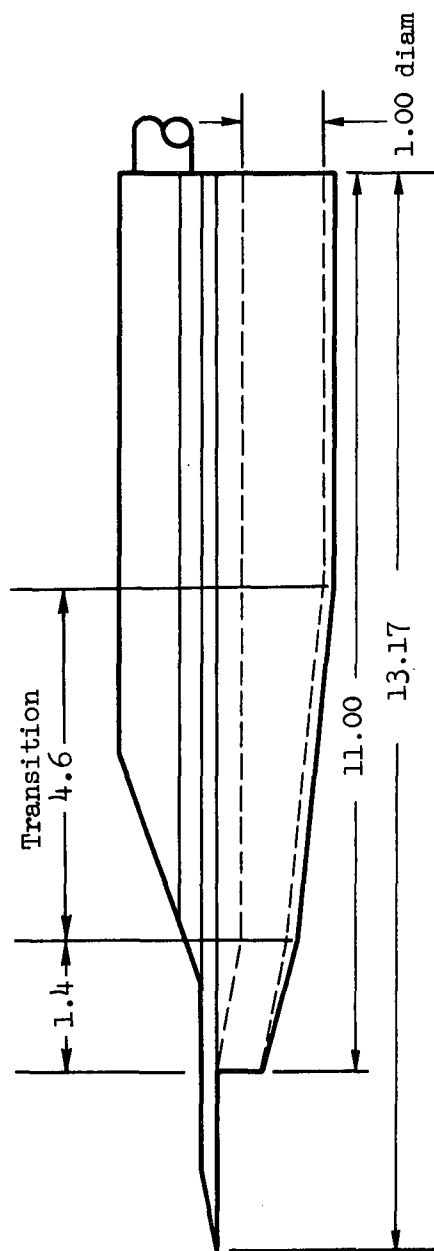
(b) Dimensions

Figure 5.- Concluded.

(a) Three-quarter front view

Figure 6.- Two-dimensional inlet duct.
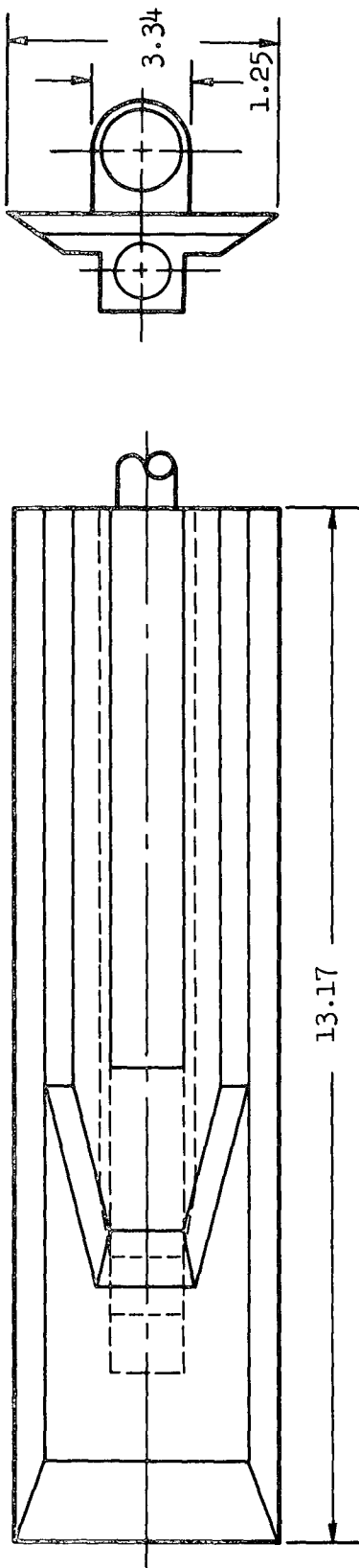
l
3.5
4.5
5.5
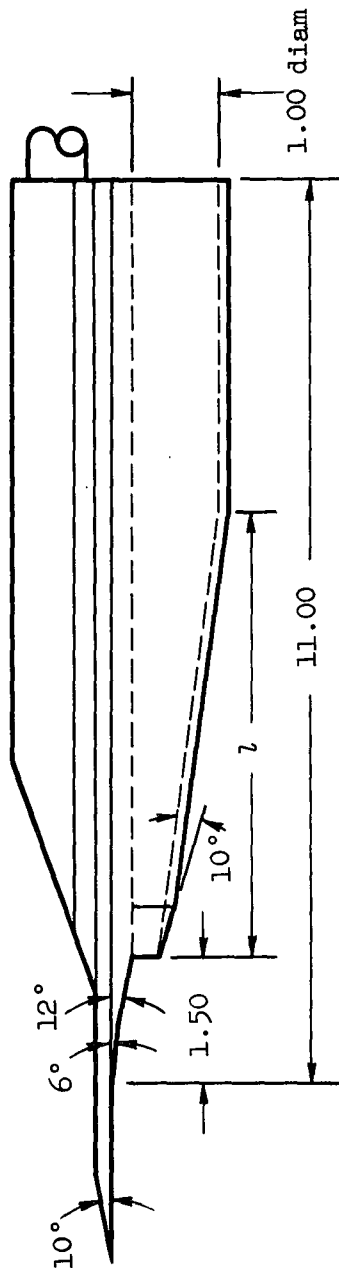
Note: All dimensions are in inches except as noted

(b) Dimensions

Figure 6.- Concluded.

Base-view

$$\frac{p_B}{p_\infty}$$

Distance from model centerline, in.
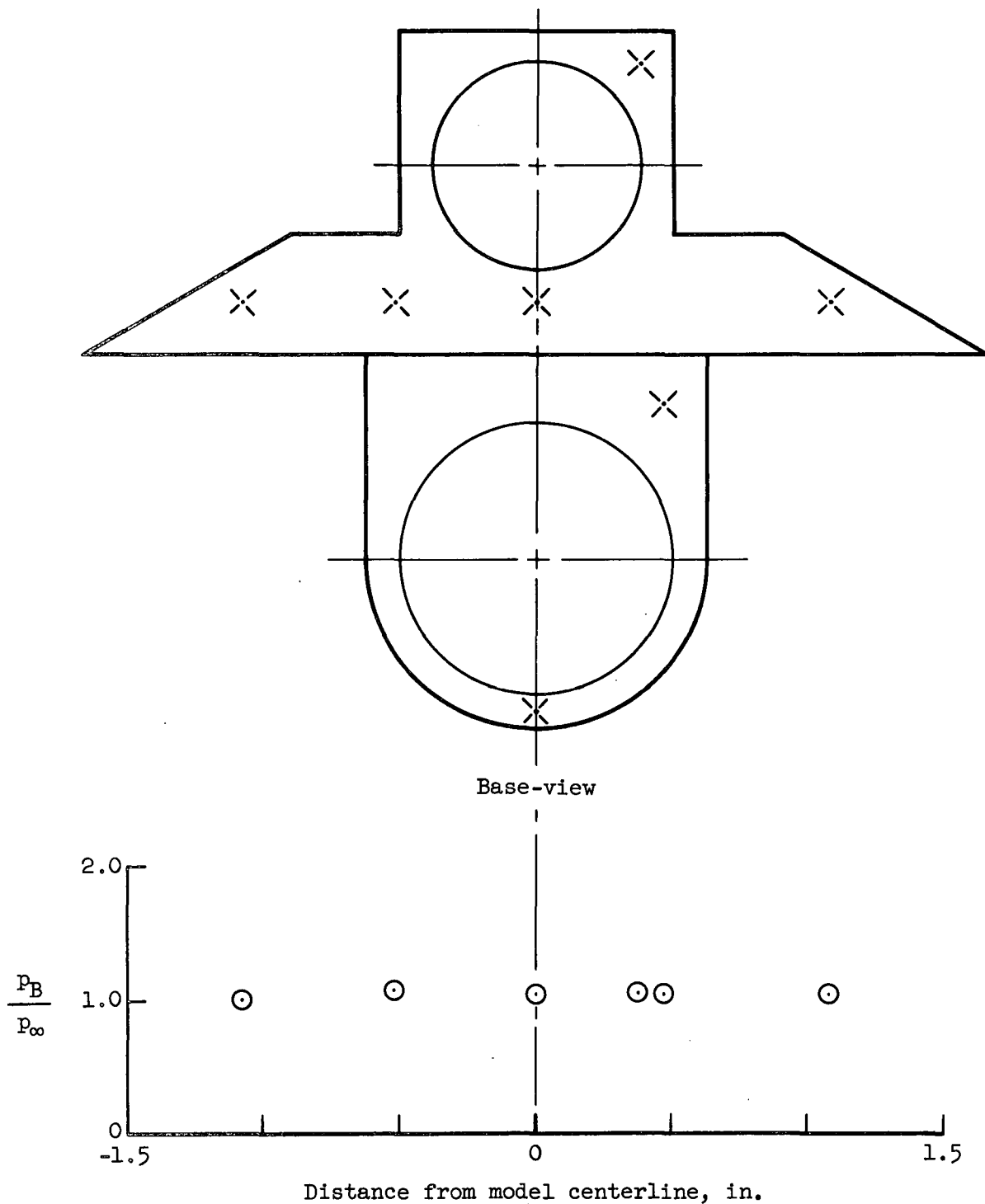
(a) Location of base-pressure measurements and measured pressure-ratio distribution for one of the circular exits; $M_\infty = 4.06$

Figure 7.- Model base pressure.

$\dfrac{\text{p}_{\text{B}}}{\text{p}_{\infty}}$

	M_{∞}
○	3.285
□	3.887
△	4.048

Base-view

Distance from model centerline, in.
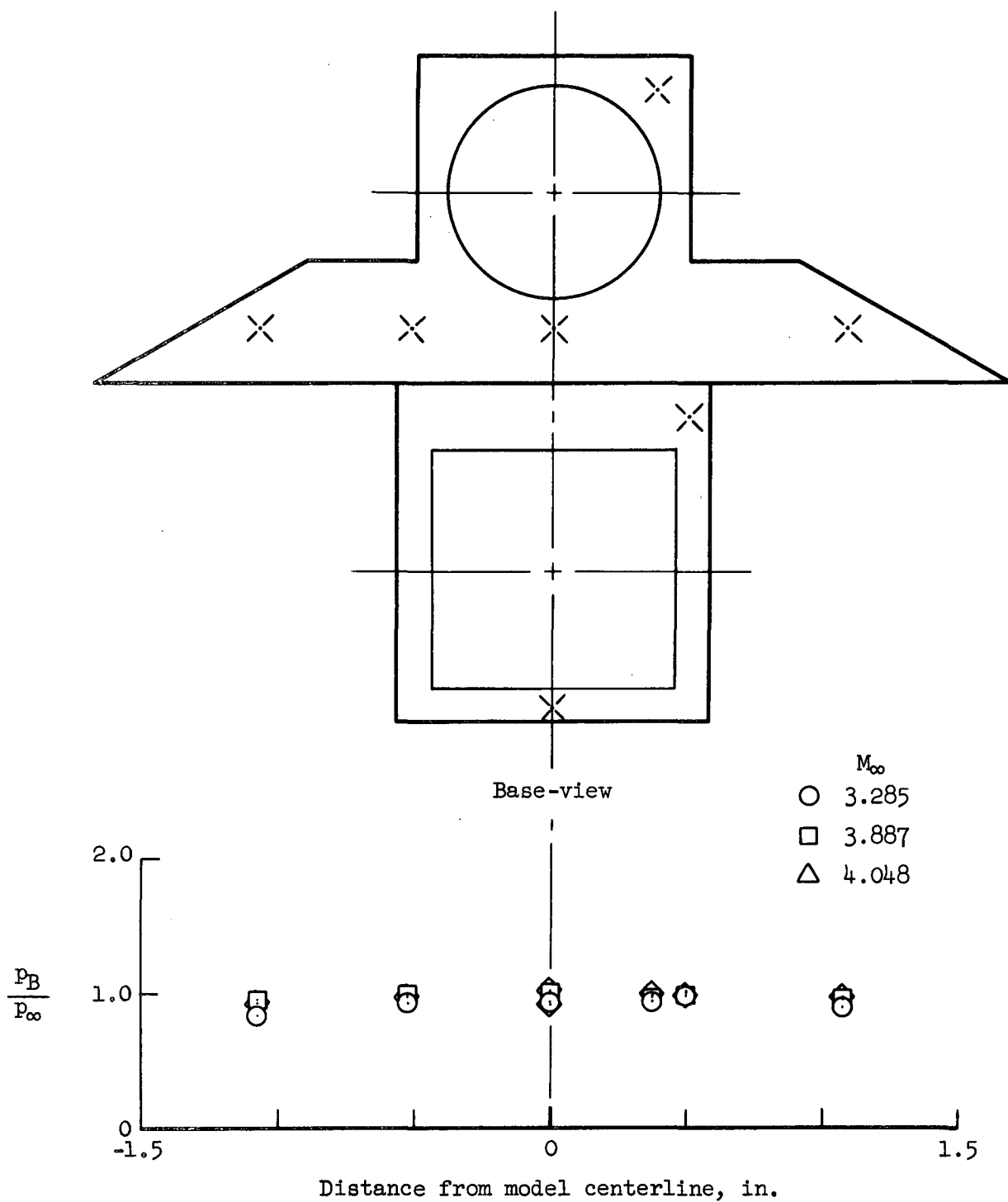
(b) Location of base-pressure measurements and measured pressure-ratio distribution for square exit

Figure 7.- Concluded.
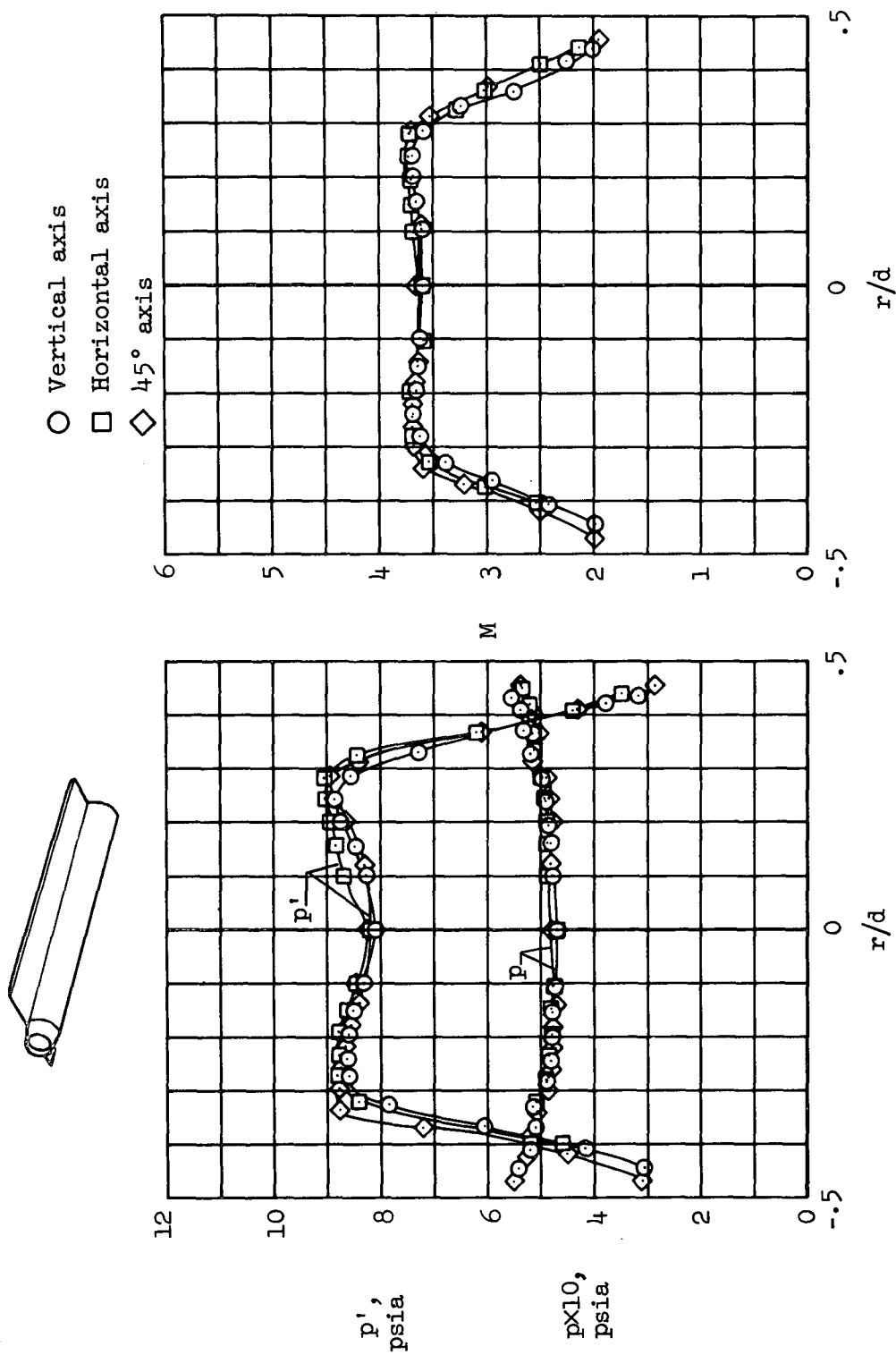
(a) Circular duct force model

Figure 8.- Duct exit flow characteristics; $\alpha = 0$, $M_\infty = 4.06$.
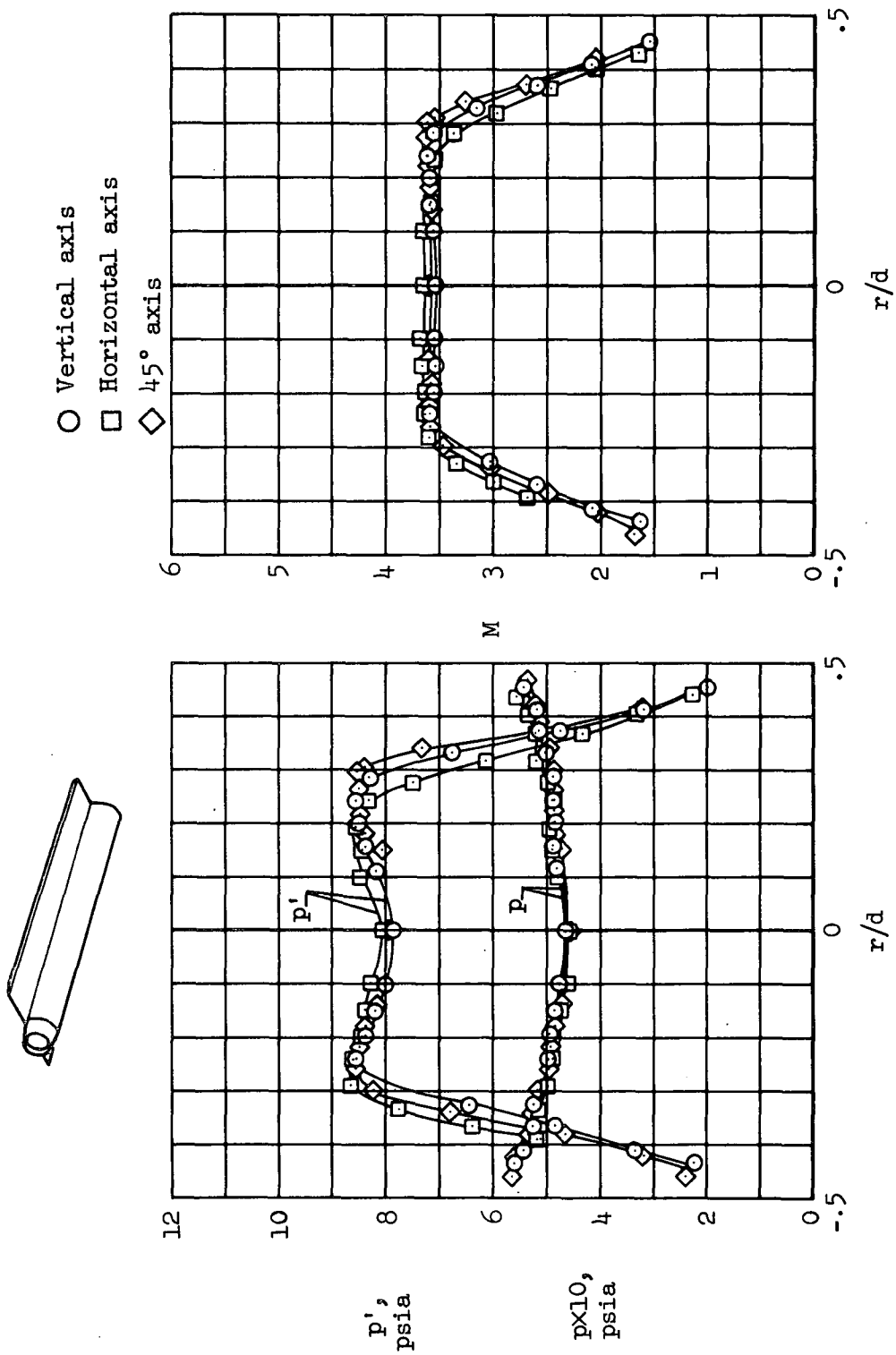
(b) Circular duct pressure model

Figure 8.- Continued.
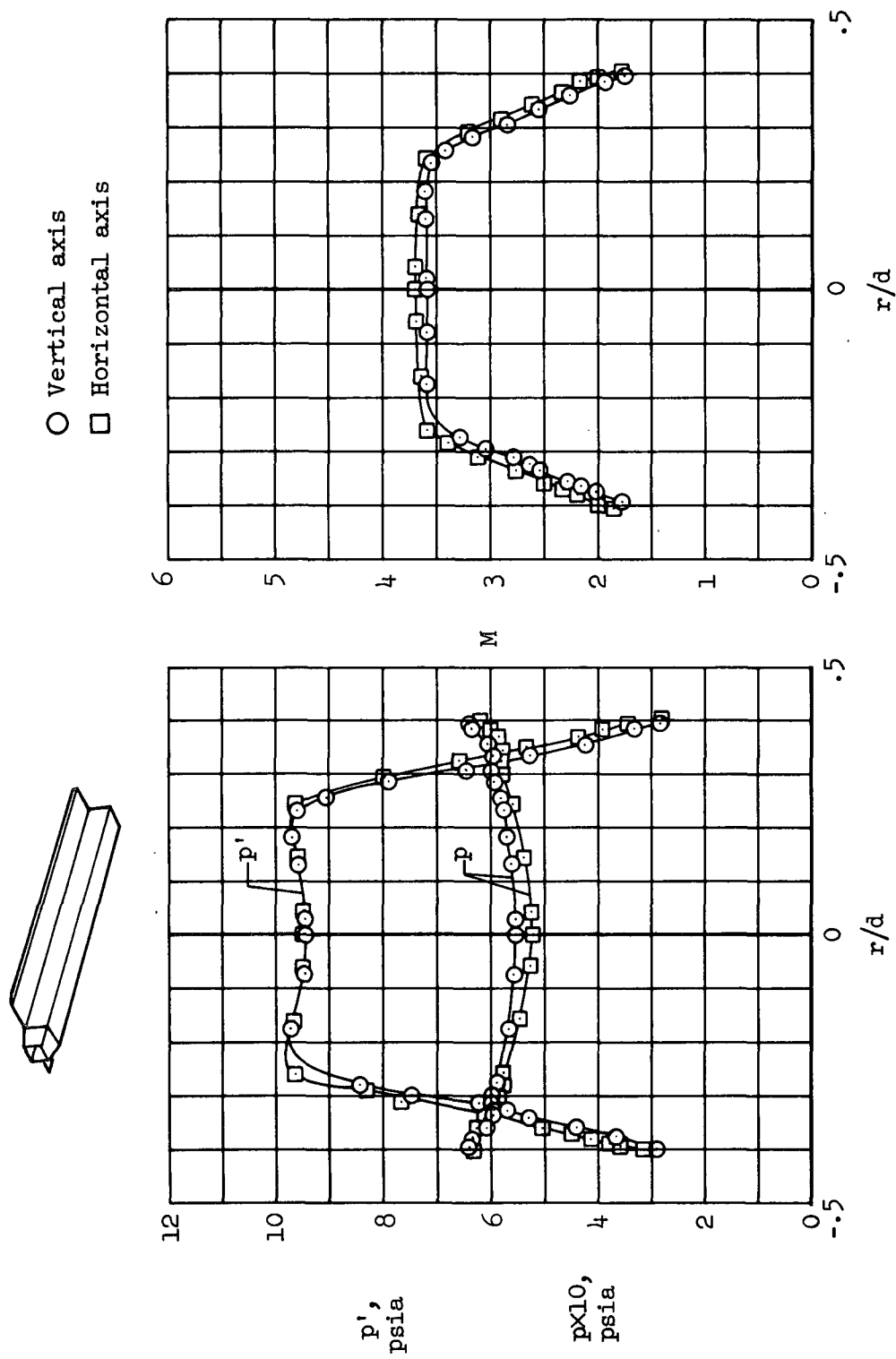
(c) Square duct pressure model

Figure 8.- Concluded.
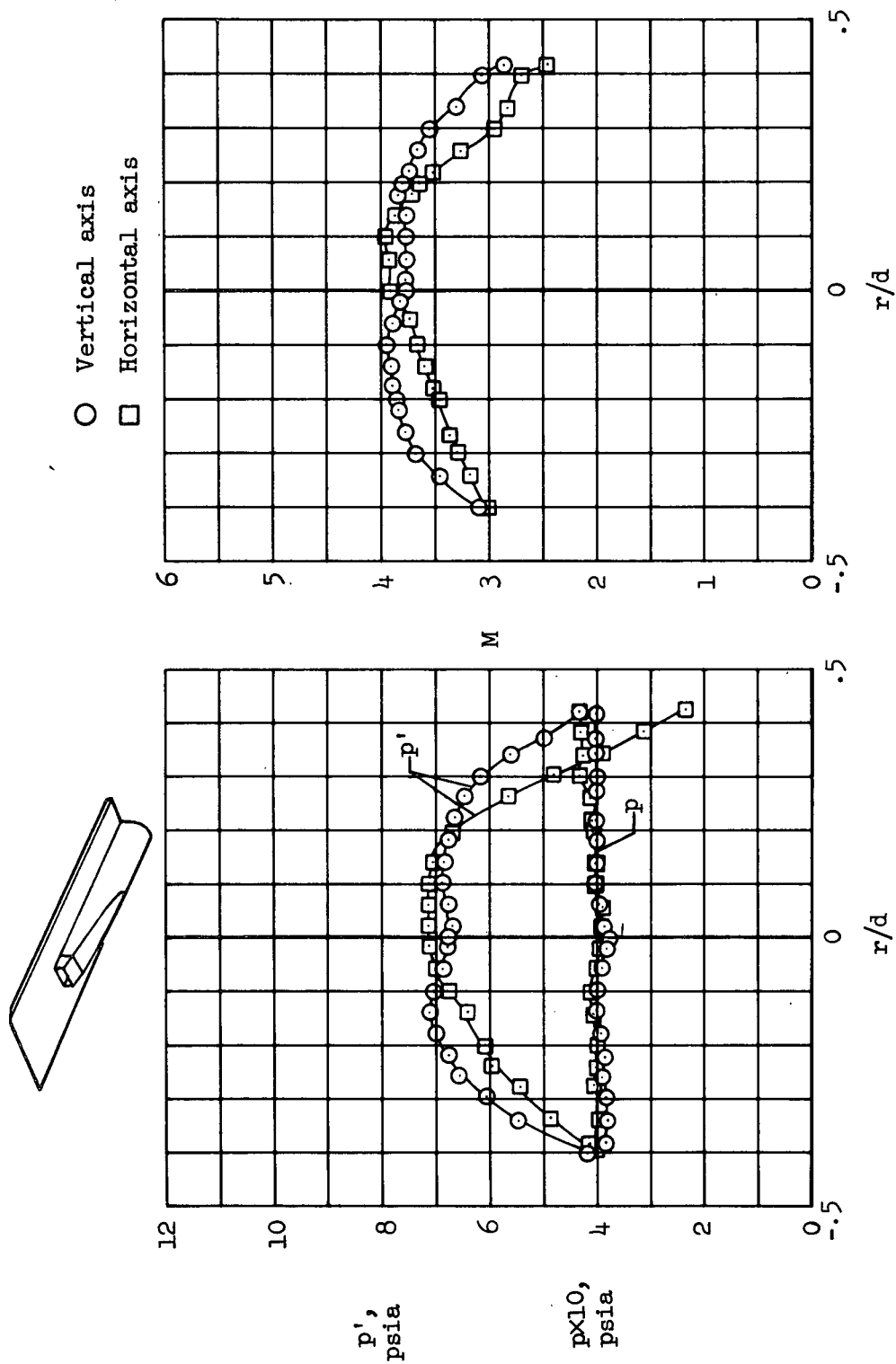
Figure 9.- Duct exit flow characteristics for the rectangular inlet duct; $\alpha = 0$, $M_\infty = 4.06$.
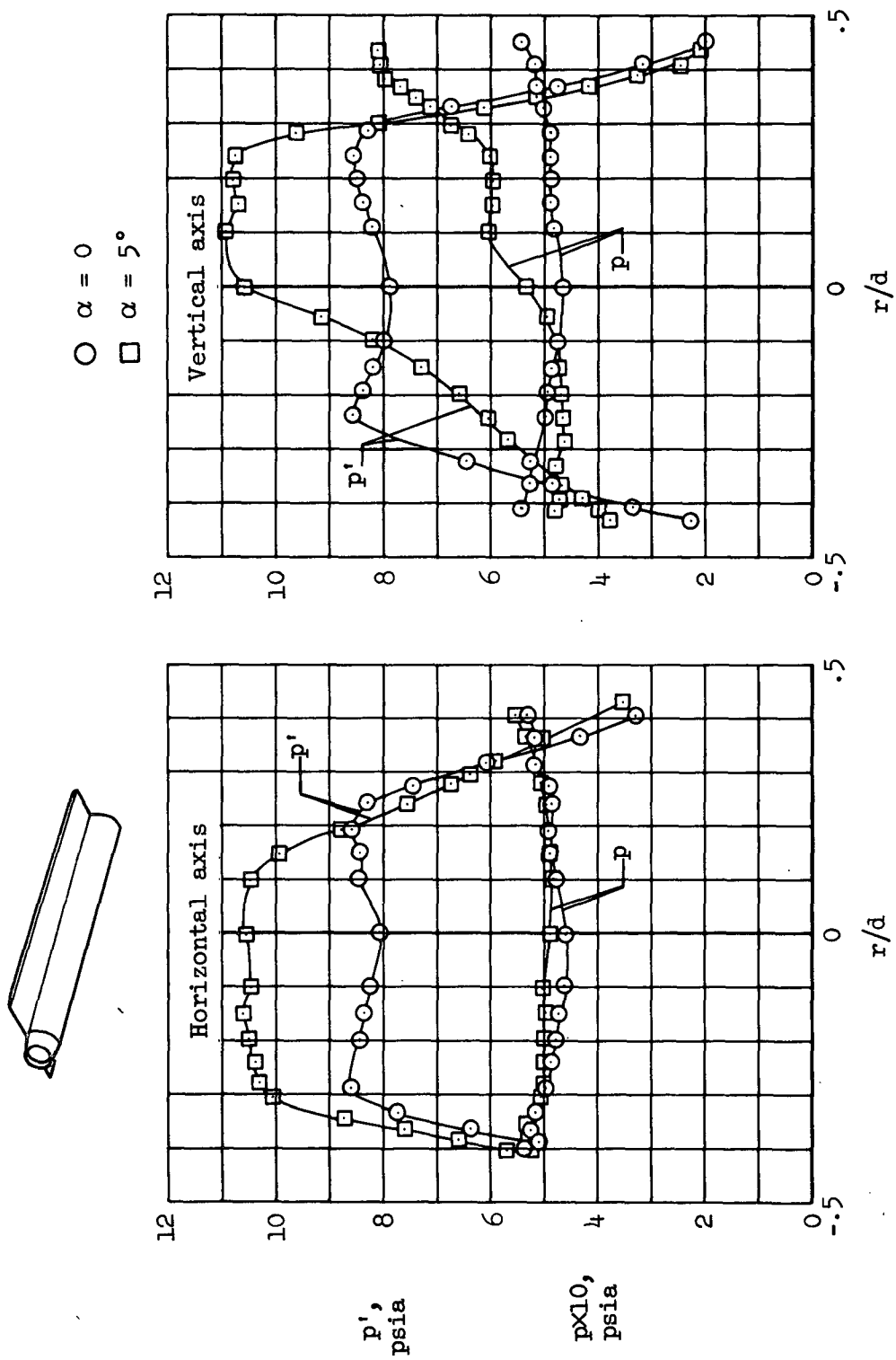
(a) Circular duct pressure model

Figure 10.- Effect of angle of attack on duct exit flow characteristics $\alpha = 0$ and $5°$, $M_\infty = 4.06$.
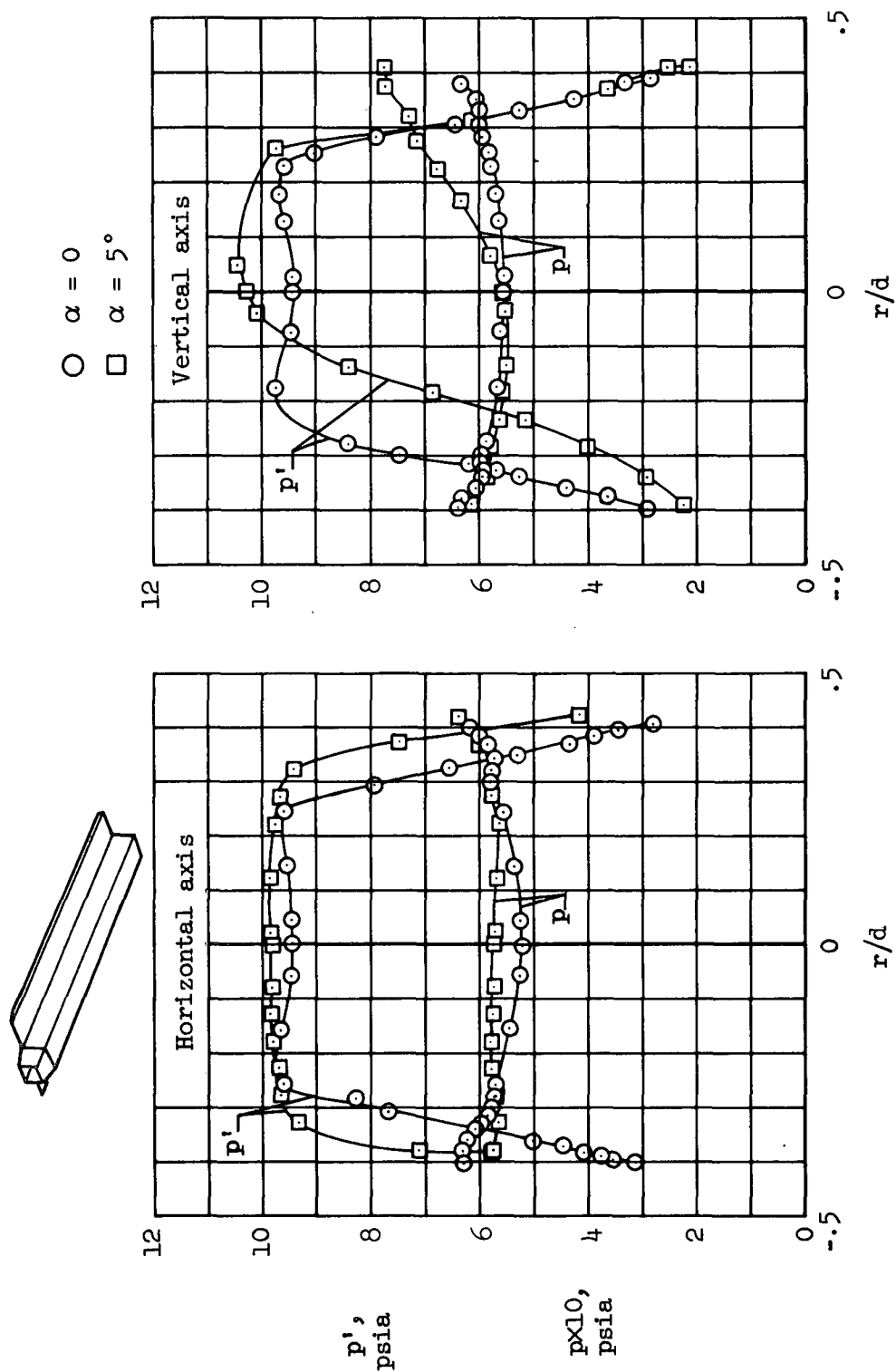
(b) Square duct model

Figure 10.- Continued.
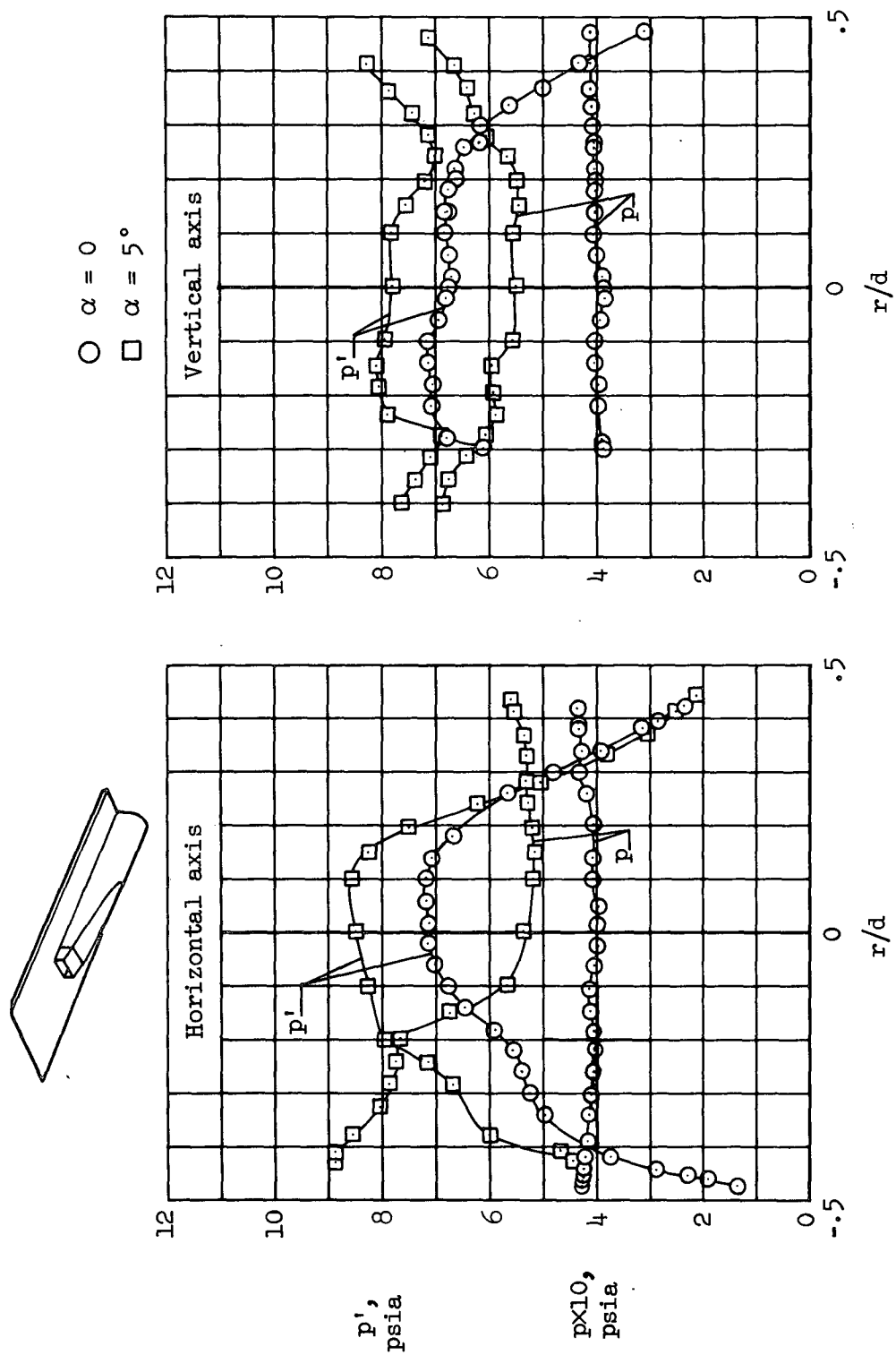
(c) Rectangular inlet duct model

Figure 10.- Continued.
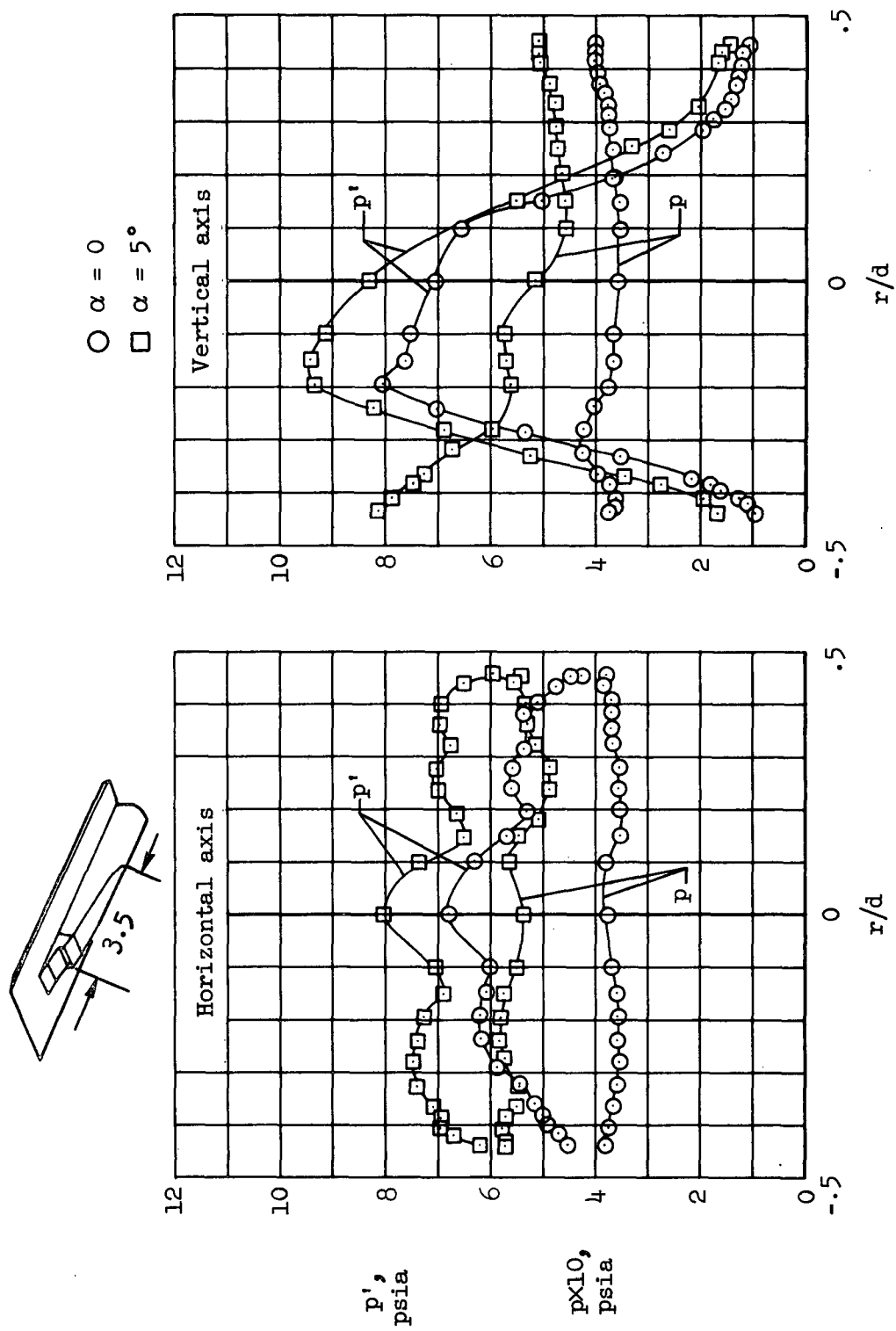
(d) Two-dimensional inlet duct model

Figure 10.- Concluded.
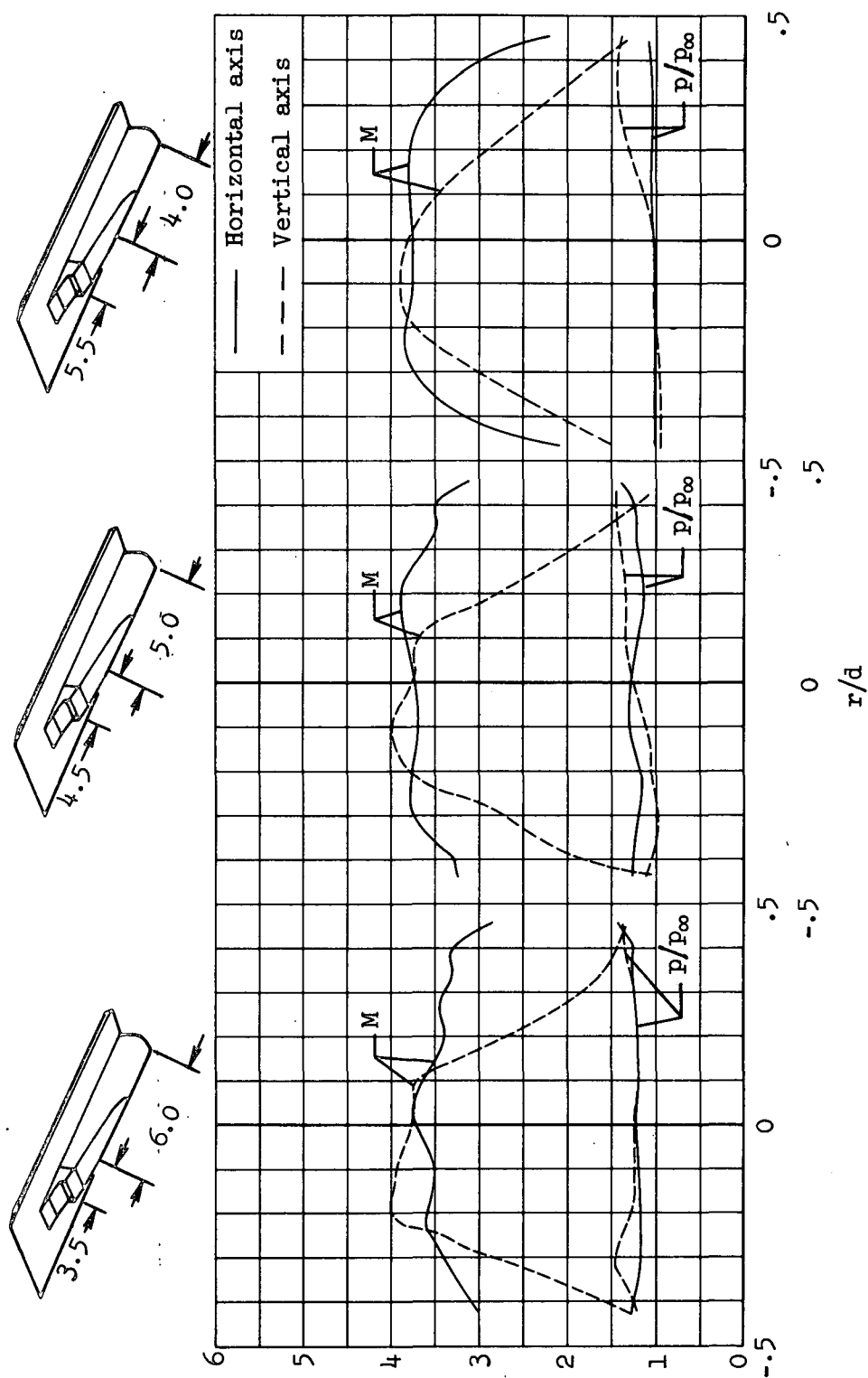
Figure 11.- Effect of transition section length on duct exit flow characteristics; $\alpha = 0$, $M_\infty = 4.06$.
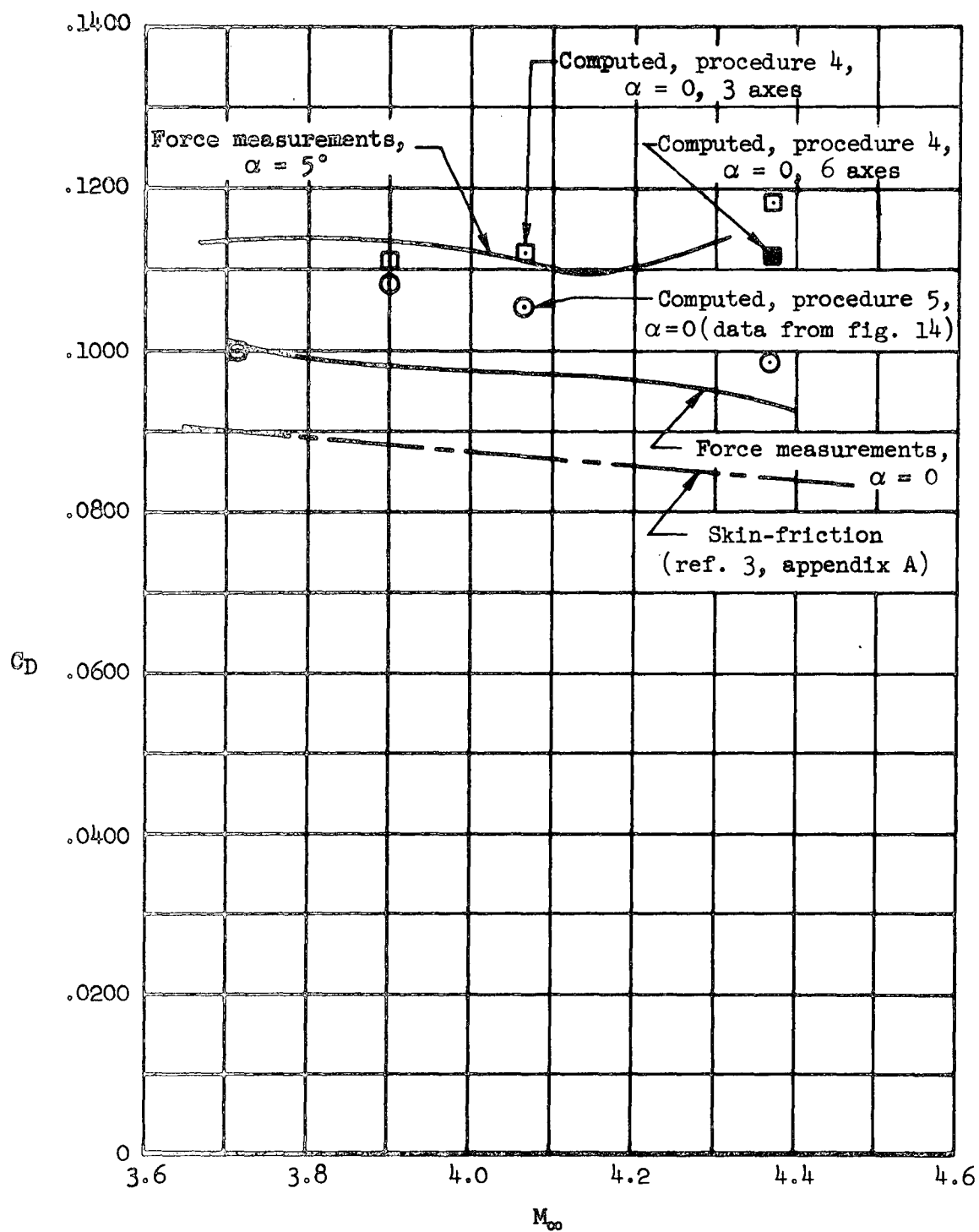
Figure 12.- Effect of Mach number on internal-drag coefficient; circular duct force model, α = 0 and 5°.
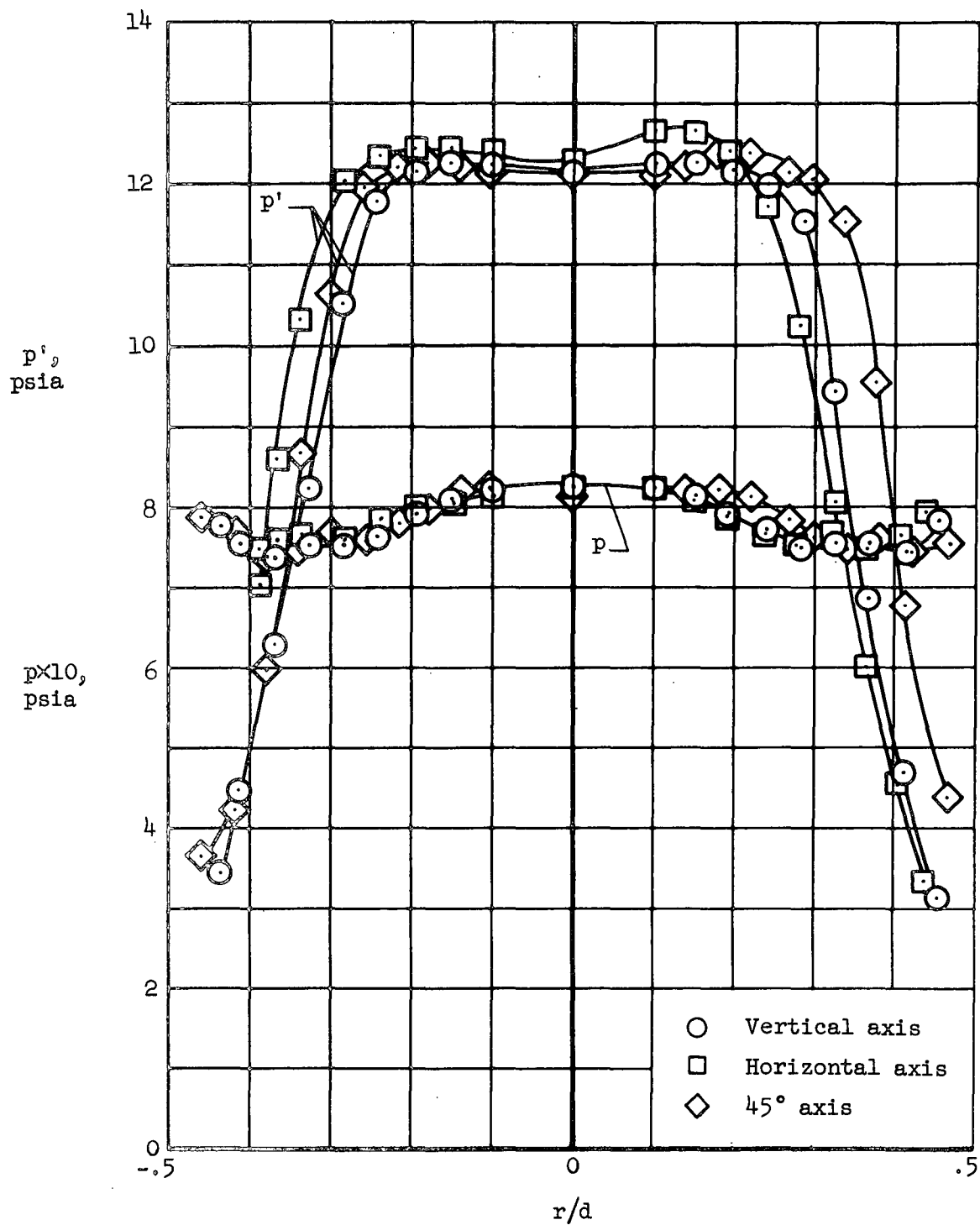
(a) $M_\infty = 3.72$

Figure 13.- Duct exit flow characteristics for circular duct pressure model; $\alpha = 0$.
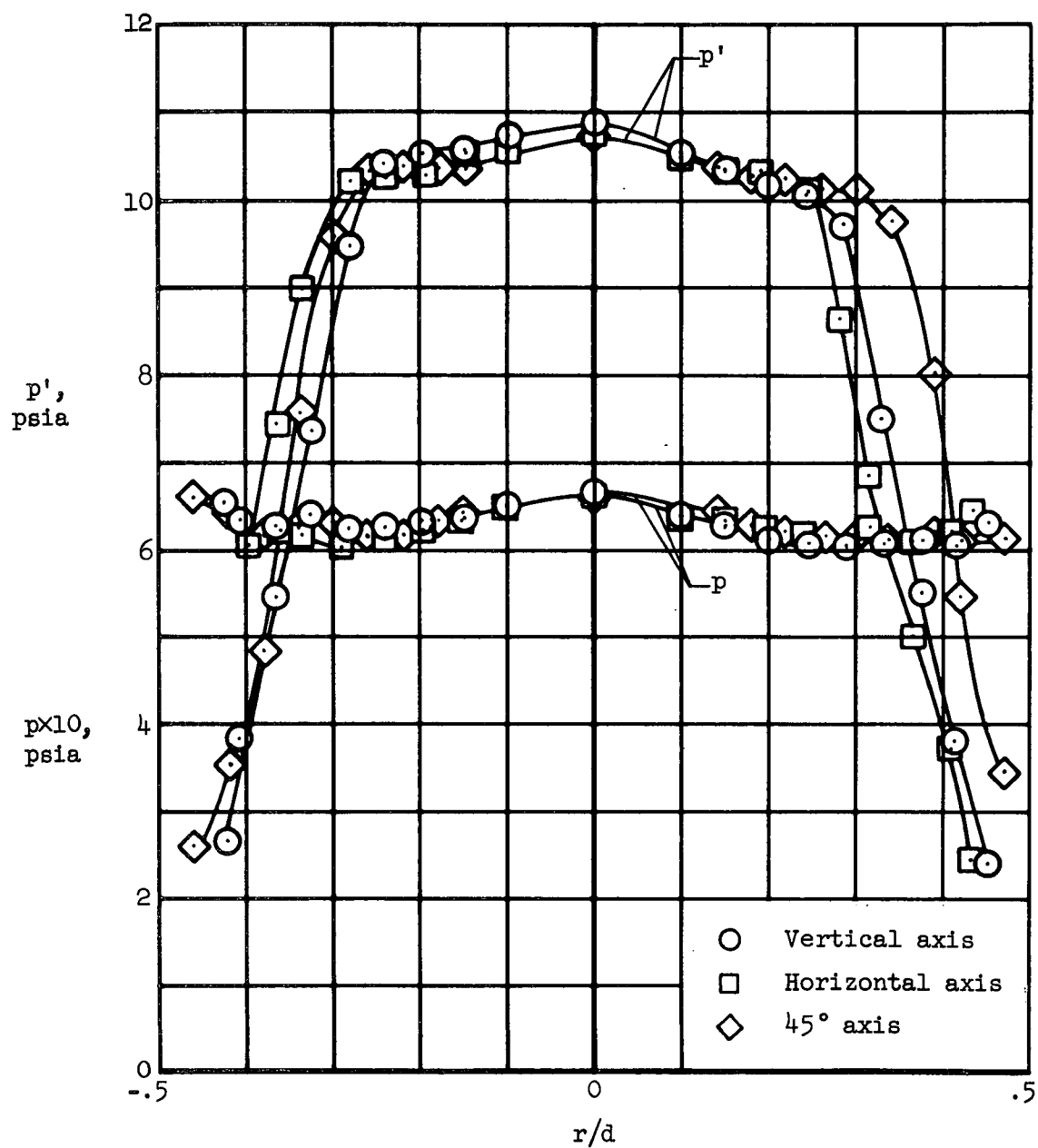
(b) $M_\infty = 3.90$
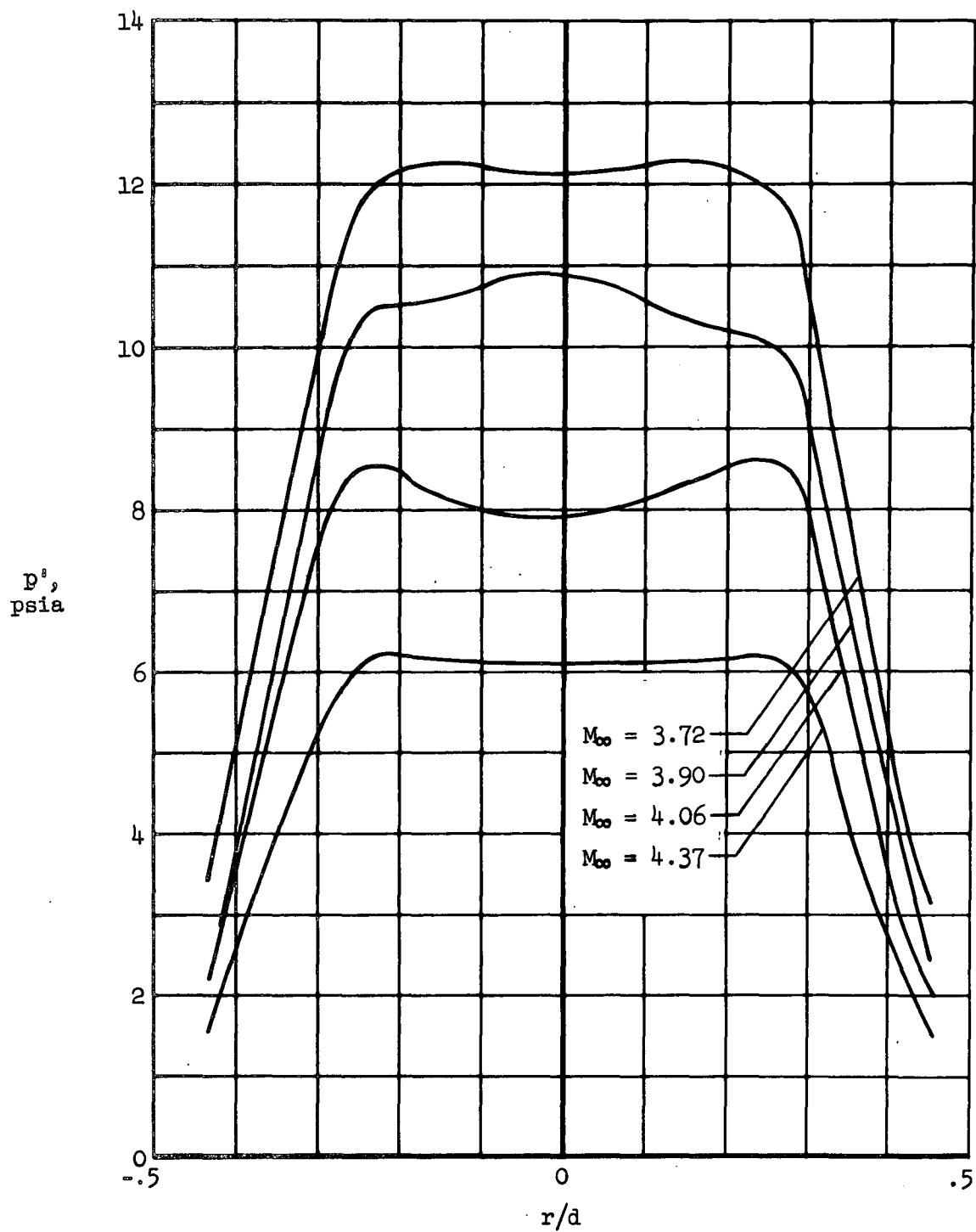
Figure 13.- Continued.
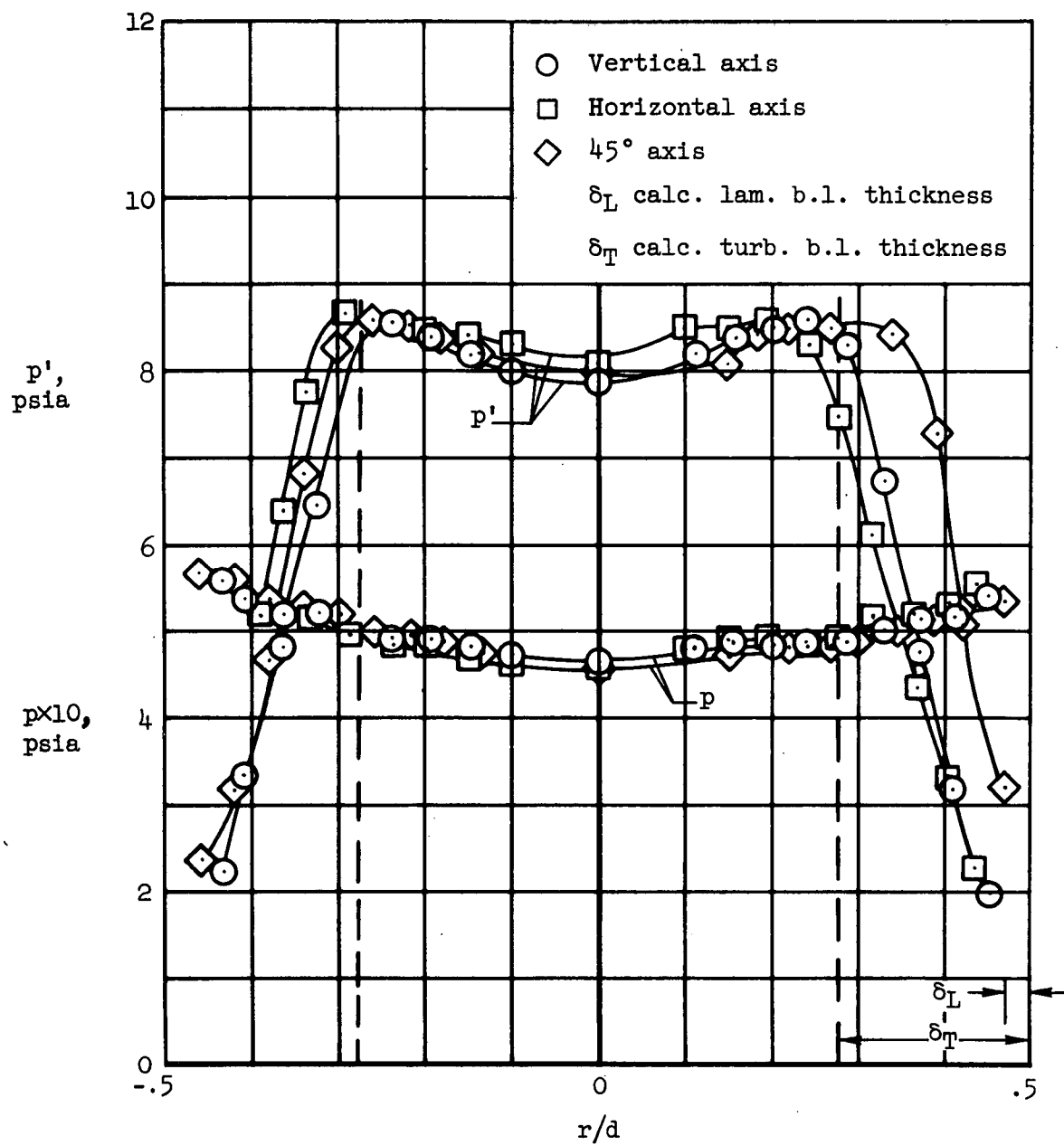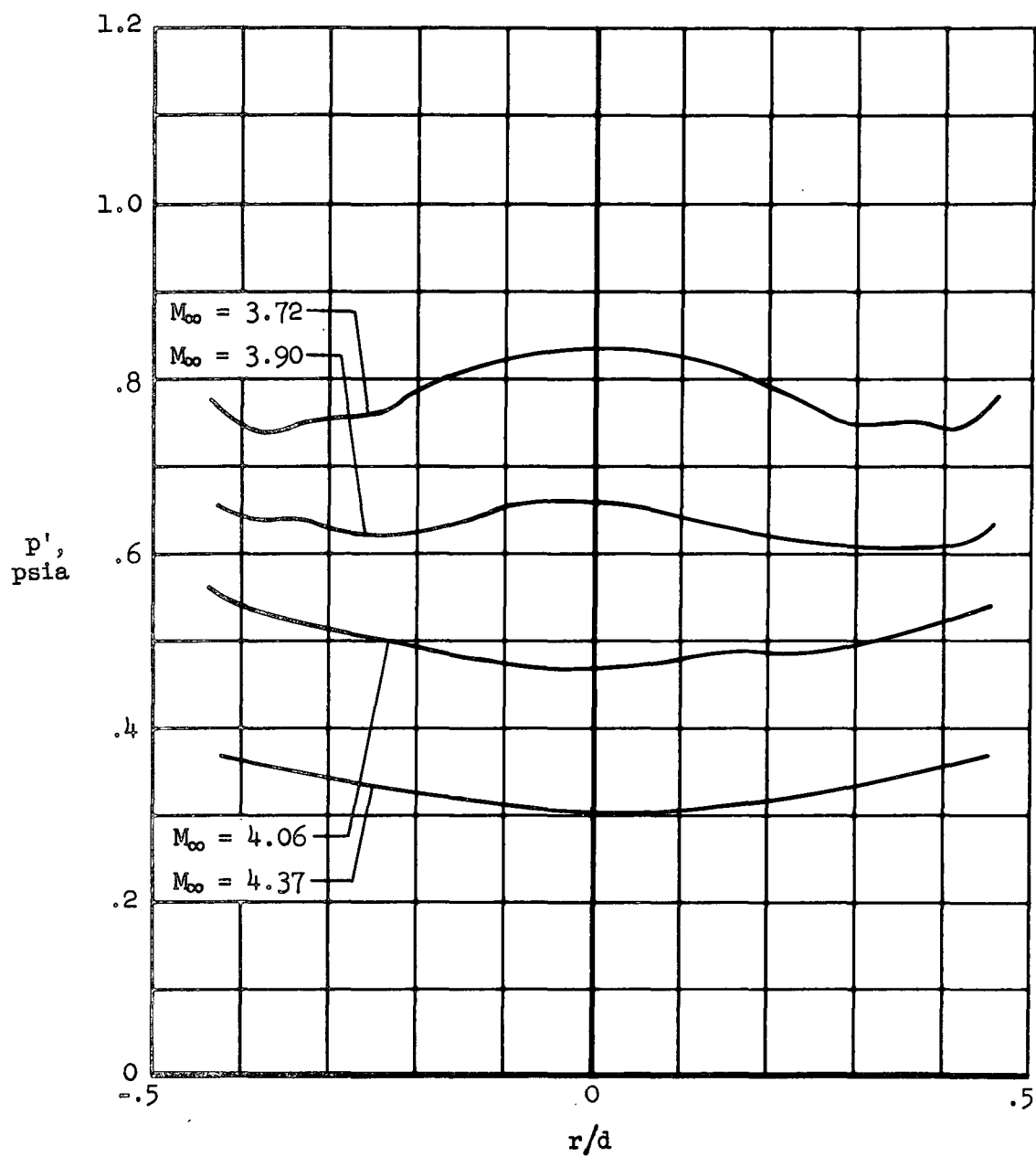
(c) $M_\infty = 4.06$

Figure 13.- Continued.

2
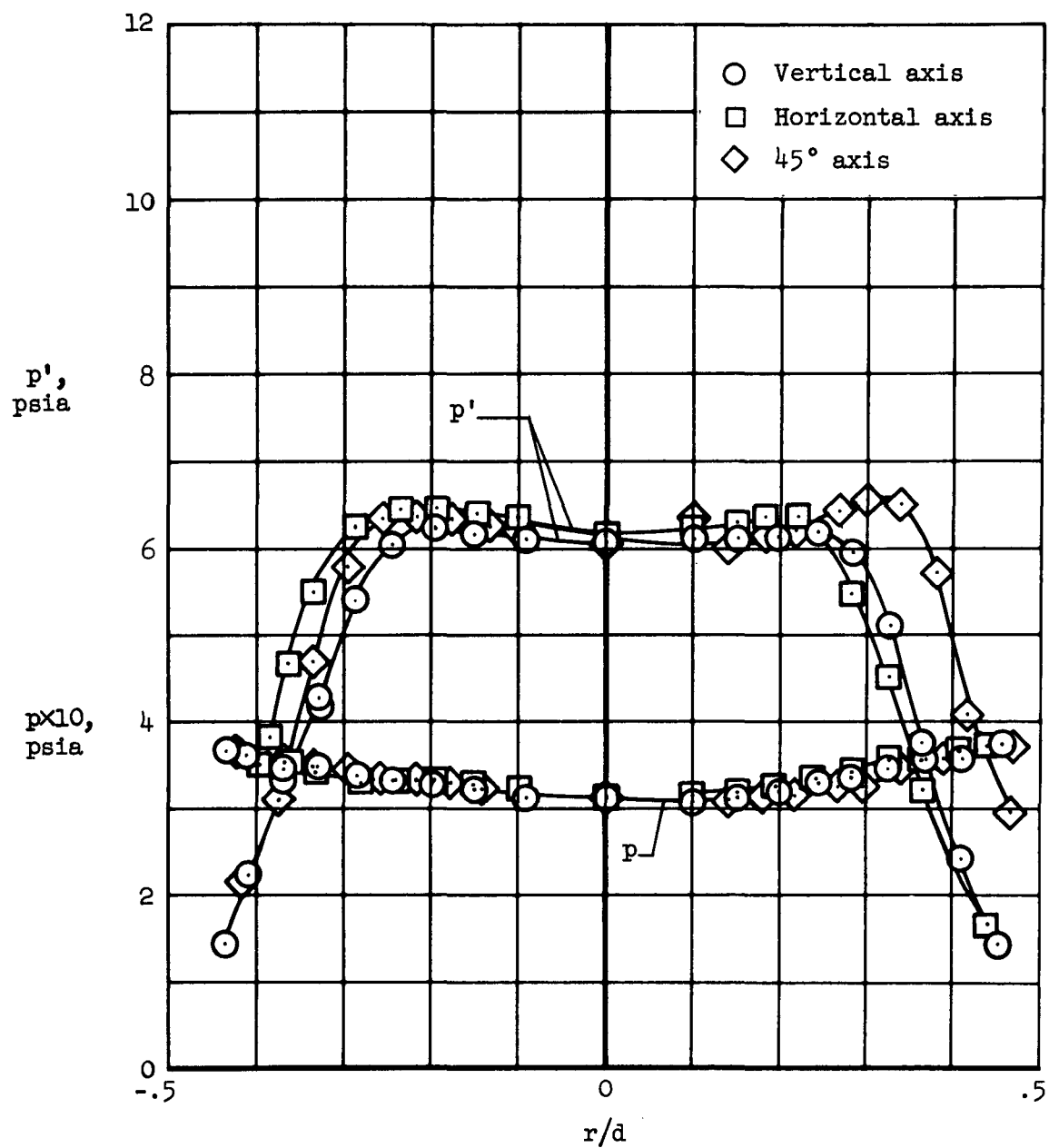
(d) $M_\infty = 4.37$

Figure 13.- Concluded.

(a) Total pressure, vertical axis

Figure 14.— Effect of Mach number on the pressure distributions; circular
duct pressure model, $\alpha = 0$.

(b) Static pressure, vertical axis
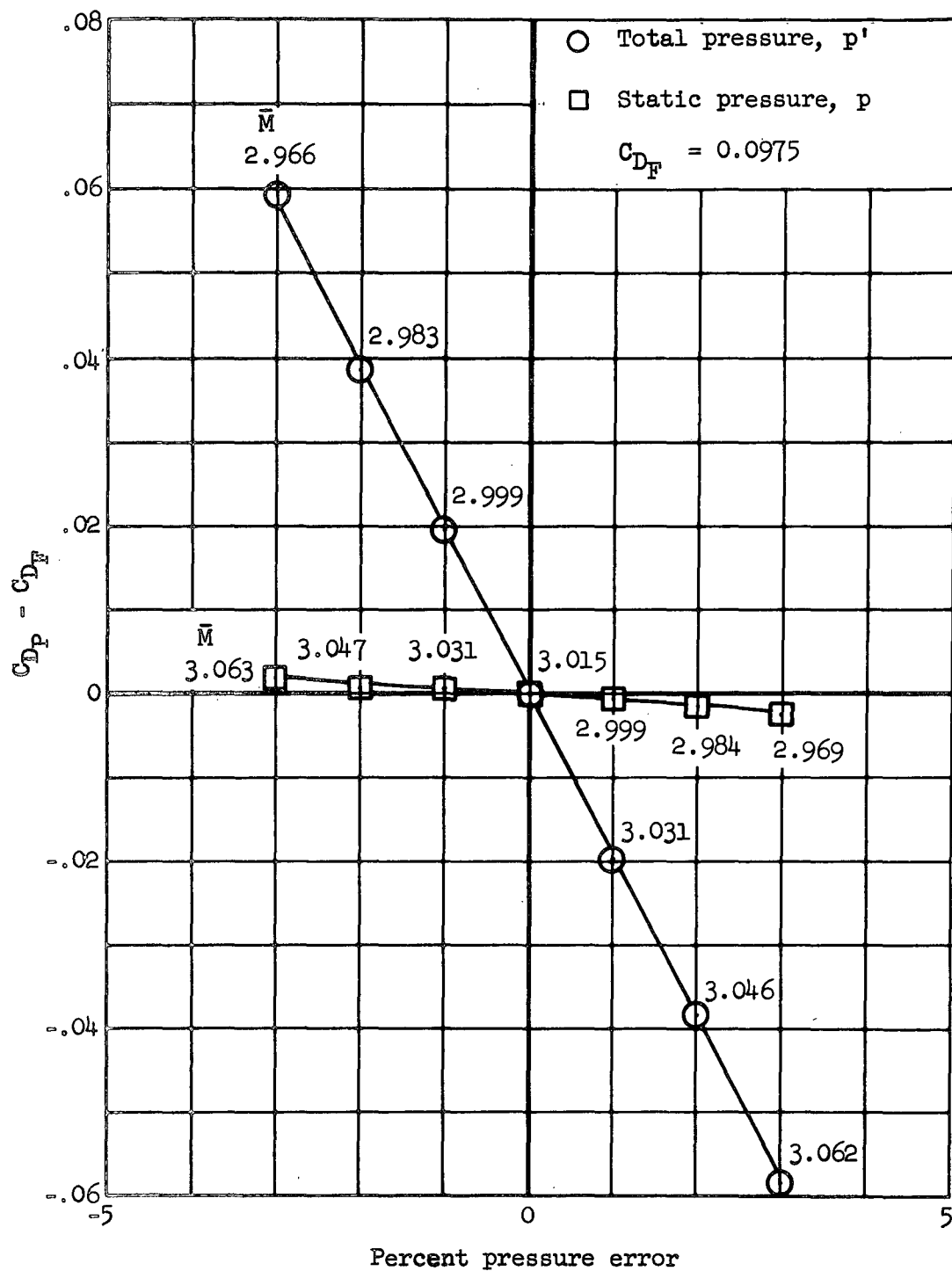
Figure 14.- Concluded.

Figure 15.- Effect of errors in static-or total-pressure measurement at the exit on internal-drag coefficient; circular duct force model, α = 0, M = 4.06.